

**A HYBRID FINITE ELEMENT/DISCRETE ELEMENT METHOD OF MODELLING  
FRACTURING OF BRITTLE ROCK BLOCKS WITH APPLICATIONS TO BLOCK  
CAVE FRAGMENTATION**

by

Kody Veltin

B.ASc., The University of British Columbia, 2017

A THESIS SUBMITTED IN PARTIAL FULFILLMENT OF  
THE REQUIREMENTS FOR THE DEGREE OF

MASTER OF APPLIED SCIENCE

in

THE FACULTY OF GRADUATE AND POSTDOCTORAL STUDIES  
(Mining Engineering)

THE UNIVERSITY OF BRITISH COLUMBIA  
(Vancouver)

November 2021

© Kody Veltin, 2021

The following individuals certify that they have read, and recommend to the Faculty of Graduate and Postdoctoral Studies for acceptance, a thesis entitled:

A Hybrid Finite Element/Discrete Element Method of Modelling Fracturing of Brittle Rock Blocks with Applications to Block Cave Fragmentation

submitted by Kody Veltin in partial fulfillment of the requirements for

the degree of Master of Applied Science

in Mining Engineering

**Examining Committee:**

Davide Elmo, Associate Professor, Mining Engineering, UBC  
Supervisor

Scott McDougall, Assistant Professor, Geological Engineering, UBC  
Supervisory Committee Member

## **Abstract**

An understanding of the fragmentation of rock blocks is an important parameter in the planning and development of a block cave mine. Traditional methods for block fragmentation analysis use empirical relationships and rule-based approaches that heavily rely on the block geometry, rather than block-to-block interactions. This thesis presents a study of fragmentation processes using a hybrid finite-element/discrete-element method (FEM/DEM). The approach is capable to account for the numerical instability generally associated with the simulation of high-velocity surface interactions and subsequent fracturing. The analysis has focused on the simulation of free-falling blocks onto a fixed surface. The initial and final block breakage has been compared against parameters including the roughness and curvature of the impacted surface, and the rock block orientation in space during free fall. The fractal relationship between resulting fragments was also explored to observe if a size invariable relationship exists and could be used for block breakage prediction.

The results show that the curvature of the impacted surface reduces the fragmentation of the rock block regardless of whether the surface is concave or convex. In addition, the angle at which the rock block contacts the impacted surface is critical with more eccentric angles resulting in less final fragmentation. Little to no correlation with the numeric JRC characterisation of surface roughness is seen. The fractal relationships show promising results for size invariability of fragmentation with some variability noticed possibly due to the mechanism of fracturing. These results could provide an increased understanding of the complexities of secondary fragmentation estimates and the range of fragmentation that could be expected in block caving.

## **Lay Summary**

Block caving is a productive mining method that uses stresses developed by gravity to break the orebody such that it naturally “caves” and the caved material can be extracted. One of the key parameters in assessing if a block cave mine is feasible is called fragmentation which is the size of the caved rock blocks. Little numerical modelling has been done to understand how a rock block may split during the fragmentation process. This thesis describes the development of a numerical model that has been used to observe the fracturing of a rock block due to gravity free-fall. Several steps have been taken to simplify these models. Models have also been developed to test the role of the orientation of the rock block and the geometry of the surface the rock block contacts. Lastly, the size invariable nature of the volumes resulting from rock block fracturing has been explored.

## **Preface**

This thesis is an original and independent work completed by the author. The author was the main author in one conference paper based on the work presented in this thesis. The thesis supervisor, Dr. Davide Elmo, co-authored this paper.

The paper “*A Hybrid FEM/DEM Approach to Estimating Rock Block Breakage due to Gravity Free-Fall*” published in the EUROCK 2021 conference proceedings and presented at the conference hosted in Turin, Italy but conducted virtually due to the COVID-19 pandemic is based on Chapters 3 and 4 of this thesis.

# Table of Contents

<b>Abstract.....</b>	<b>iii</b>
<b>Lay Summary .....</b>	<b>iv</b>
<b>Preface.....</b>	<b>v</b>
<b>Table of Contents .....</b>	<b>vi</b>
<b>List of Tables .....</b>	<b>ix</b>
<b>List of Figures.....</b>	<b>x</b>
<b>Acknowledgements .....</b>	<b>xiii</b>
<b>Chapter 1: Introduction .....</b>	<b>1</b>
1.1    Background.....	1
1.2    Research Objectives.....	3
1.3    Thesis Organization .....	4
<b>Chapter 2: Literature Review.....</b>	<b>6</b>
2.1    Introduction.....	6
2.2    Brittle Rock Failure.....	6
2.2.1    Brittle Fracture Theory .....	7
2.2.2    Mohr-Coulomb Failure Criterion.....	8
2.2.3    Hoek-Brown Failure Criterion .....	9
2.2.4    Rock Fracture in Massive to Moderately Jointed Rockmasses .....	11
2.3    Methods for Estimating Fragmentation .....	14
2.3.1    Block Cave Fragmentation (BCF) Software.....	15
2.3.1.1 <i>In Situ</i> and Primary Fragmentation from BCF.....	15

2.3.2	Secondary Fragmentation from BCF .....	20
2.3.3	Discrete Fracture Network (DFN) Models .....	26
2.3.3.1	<i>In Situ</i> Fragmentation from DFN Models.....	28
2.3.3.2	Primary Fragmentation from DFN Models.....	31
2.3.3.3	Secondary Fragmentation from DFN Models.....	32
2.4	Hybrid Finite Element/Discrete Element Modelling .....	34
2.4.1	ELFEN Input Parameters.....	35
2.4.1.1	Material Strength Parameters.....	35
2.4.1.2	Contact Parameters .....	37
2.5	Chapter Summary .....	39
<b>Chapter 3: Hybrid Finite Element/Discrete Element Model Development.....</b>		<b>41</b>
3.1	Base Case Model Development.....	41
3.2	Base Case Model Results.....	48
3.3	Damping Sensitivity.....	49
3.4	Chapter Summary .....	53
<b>Chapter 4: Geometric Study.....</b>		<b>55</b>
4.1	Block Rotation .....	55
4.2	Surface Curvature .....	57
4.3	Surface Roughness.....	58
4.4	Chapter Summary .....	63
<b>Chapter 5: Fractal Block Breakage Relationships .....</b>		<b>65</b>
5.1	Chapter Summary .....	70
<b>Chapter 6: Conclusion.....</b>		<b>71</b>

6.1	Research Summary .....	71
6.2	Main Findings and Conclusions .....	72
6.3	Limitations and Assumptions .....	73
6.4	Recommendations for Future Work.....	74
	<b>Bibliography .....</b>	<b>76</b>

## List of Tables

Table 1: BCF Cave Weight Percentage by Active Draw Column Geometry (Based on Esterhuizen, 2005). .....	23
Table 2: BCF Probability of Splitting by Aspect Ratio (Based on Esterhuizen, 2005).....	24
Table 3: BCF Probability of Splitting of Combined Blocks by Aspect Ratio (Based on Esterhuizen, 2005). .....	25
Table 4: BCF Cushioning Adjustment by Percentage of Fines (Based on Esterhuizen, 2005)....	26
Table 5: FEM/DEM Model Material Parameters. ....	44
Table 6: FEM/DEM Modelling Parameters.....	45

## List of Figures

Figure 1: Schematic of a typical block cave layout showing the undercut and production (extraction) levels (adapted from Brown (2003)).	2
Figure 2: Fracture Propagation in the Direction of Maximum Principal Stress (Eberhardt et al., 1998)	7
Figure 3: Mohr-Coulomb Failure Criterion (Labuz & Zang, 2012)	9
Figure 4: Mohr-Coulomb fit to Hoek-Brown Curve (Hoek et al., 2002)	11
Figure 5: GSI Chart with Grey Shaded Region Showing Rockmasses for which Hoek-Brown Strengths are not Applicable (Cai et al., 2004)	12
Figure 6: a) Trilinear Failure envelope (red) relative to Hoek-Brown Failure Criterion and b) Equivalent Non-Linear Fit to the Tri-Linear Envelope (Bewick et al., 2019)	13
Figure 7: Flow Chart of BCF Primary Fragmentation Process	17
Figure 8: Formation of a Combined Block in BCF (Esterhuizen, 2005)	18
Figure 9: Probability Relationships Used in BCF Software for a) Joint Condition Probability of Separation and b) Block Weight Probability of Separation (Esterhuizen, 2005)	19
Figure 10: Flow Chart of BCF Secondary Fragmentation Process	21
Figure 11: FracMan $P_{ij}$ intensity classification scheme (based on Dershowitz et al., 1998)	28
Figure 12: Example of the Sybil Frac Algorithm used on a DFN Model showing a) The Initial DFN b) The Fractures Mapped onto the specified grid c) blocks mapped into the grid and d) the final block blocks formed (Elmo et al., 2014)	30
Figure 13: Results of the FEM/DEM Modelling of Primary Fragmentation for the 10th, 50th, and 90th Percentile of P32 Intensity (Rogers et al., 2010)	31

Figure 14: FEM/DEM Modelling of Rock Blocks within a Cave with Different Defect Intensities  
a) Intact Blocks b) Blocks with Randomly Oriented Defects, and c) Blocks with Defects at a  
Constant Orientation (Rogers et al., 2010) ..... 33

Figure 15: a) Fracture Plane Direction from the Rankine Rotating Crack Model, b) Intra-element  
Fracturing and c) Inter-element Fracturing (Klerck et al., 2004). ..... 37

Figure 16: Schematic of Contact Field and Search Zone FEM/DEM Parameters (Not to Scale).39

Figure 17: FEM/DEM Base Case Model Geometry Showing Rock Block, Hopper, and  
Triangular Mesh..... 42

Figure 18: ELFEN Model without Deletion Sequence Showing Highly Deformed, High Speed  
Modelling Artefact..... 47

Figure 19: Results of the Base Case FEM/DEM Model. a) Initial Rock Block Breakage at First  
Hopper Contact, b) Final Rock Block Breakage at Model Equilibrium and c) Percent Passing  
Chart Showing Initial and Final Fragmentation..... 49

Figure 20: Results of the Contact Damping Sensitivity Models. a) Initial Hopper Contact, b)  
Final Model Equilibrium. c) ELFEN Rock Block Visualisations. .... 51

Figure 21: Results of the Top Frequency Damping Sensitivity Models. a) Initial Hopper Contact,  
b) Final Model Equilibrium. c) ELFEN Rock Block Visualisations. .... 52

Figure 22: Results of the Rigid Body Motion Damping Sensitivity Models. a) Initial Hopper  
Contact, b) Final Model Equilibrium. c) ELFEN Rock Block Visualisations..... 53

Figure 23: Results of the Block Rotation Models a) Initial Hopper Contact ELFEN  
Visualisations, b) Final Model Equilibrium ELFEN Visualisations, c) Initial Block Size  
Percentiles by Rotation Angle, and d) Final Block Size Percentiles by Rotation Angle..... 56

Figure 24: Results of the Surface Concavity Testing. a) Initial Hopper Contact, b) Final Model Equilibrium. c) ELFEN Rock Block Visualisations. ....	58
Figure 25: Joint Roughness Coefficient Profiles (Barton and Choubey 1977) .....	59
Figure 26: Joint Roughness Coefficient Scaling Chart (Barton, N., Bandis, 1982) .....	60
Figure 27: Surface Roughness Model Geometry a) JRC Hopper Surfaces b) 45-degree Block Orientation over JRC = 18 Surface and c) 0-degree Block Orientation over JRC = 18 Surface..	61
Figure 28: Results of Surface Roughness Models a) Initial Block Contact for 45-degree Rotation Models b) Final Model Equilibrium for 45-degree Rotation Models c) Initial Block Contact for 0-degree Rotation Models, and d) Final Model Equilibrium for 0-degree Rotation Models. ....	62
Figure 29: Variable Size Models .....	65
Figure 30: Log-Log Plot of Final Size Distribution of Variable Size Models with Power Law Fit .....	67
Figure 31: Log-Log Plot of Block Rotation Models.....	68
Figure 32: Log-Log Plot of Surface Curvature Models.....	69
Figure 33: Log-Log Plot of Surface Roughness Models .....	69

## **Acknowledgements**

I would like to express my gratitude to the faculty, staff, and students at UBC, who have supported me to continue my research amongst the context of the COVID-19 global pandemic. I am grateful for the support of my supervisor Dr. Davide Elmo who has been patient, understanding, and encouraging throughout this process.

I would also like to thank my colleagues at Golder Associates Ltd. for providing support (and income) throughout my degree.

Special thanks to my partner, Jeremy Lotto, for helping me become a better scientist.

## **Chapter 1: Introduction**

### **1.1 Background**

As the demand for mining resources becomes higher, more mining operations are transitioning to efficient, cost-effective, methods of mining large underground orebodies. A common method for efficient mining is “cave mining” which includes a particular method of mining called block caving. “Cave mining” refers to all mining operations where the orebody caves naturally after undercutting. Drawpoints are used to recover the caved material (D. Laubscher, 2000). Block caving specifically refers to a mining method for which an approximately equidimensional block of ore is fully undercut to create a void to initiate caving (Brown, 2003). Initiation of caving is done by progressively blasting panels beneath the block being mined to develop an undercut level. The undercut level is connected to an extraction level by bell-shaped openings called drawbells connected to several drawpoints. The drawbells allow caved ore to pass from the undercut level to the drawpoints, where it is collected and transported to be processed. The growth of the cave continues as ore is removed and fractures progress due to induced fracturing by stress redistribution and gravity. Figure 1 shows a schematic example of a block cave mine.

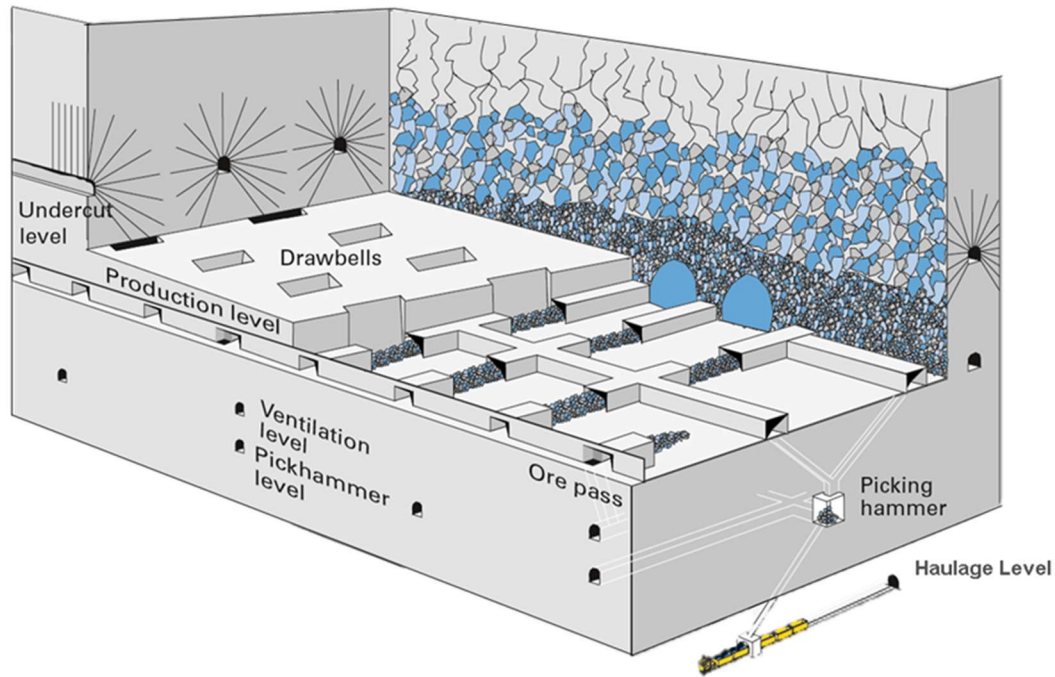


**Figure 1: Schematic of a typical block cave layout showing the undercut and production (extraction) levels (adapted from Brown (2003)).**

Block cave methods are low cost and highly productive, however, the capital expenditure related to infrastructure and development before production can be very high. As such, a proposed block cave mine requires a strong understanding of the geological and geotechnical characteristics related to the orebody to be confident in the caveability. One of the key factors for the feasibility of a block cave mine is the fragmentation which refers to the size distribution of the rock blocks generated and reporting to the drawpoints (Brown, 2003; D. Laubscher, 2000). Fragmentation is divided into three stages depending on temporal-spatial conditions: *in situ* fragmentation, primary fragmentation, and secondary fragmentation. *In situ* fragmentation is the fragmentation of the pre-mined rock mass due to natural rock fractures. Primary fragmentation is developed by induced fracturing due to the redistribution of stresses as the cave progresses

upwards. Secondary fragmentation is caused by rock block movement through the ore column to the drawbells resulting in rock block attrition (Brown, 2003).

The expected fragmentation of a block cave mine is a key decision parameter when determining the feasibility of such projects (D. Laubscher, 2000; D. H. Laubscher, 1994). The reduced block size due to block splitting may aid in the flow of the ore column and reduce the potential for rock blocks to obstruct drawpoints (hang-ups). Smaller rock blocks are also easier and more cost-effective to transport and process. (Ngidi & Pretorius, 2010).

In recent years, there has developed an interest in mining stronger, more competent, orebodies using block caving methods, rather than caving being limited to weak rock that readily fragments (Chitombo, 2010; D. H. Laubscher, 1994).

## **1.2 Research Objectives**

Prediction of orebody fragmentation is a critical element in determining the feasibility of a block cave mine and is important for mine design and planning. Prediction of fragmentation, particularly secondary fragmentation, is often based on empirical relationships rather than modelling. As block caves are continually being proposed in stronger, more brittle, rock masses, there is a genuine need for a method to model the fracturing of brittle rock blocks in highly dynamic situations like the conditions seen during secondary fragmentation processes. In addition, the currently popular methods for determining fragmentation conclude with the assumption that if a block splits during secondary fragmentation, it will split perfectly, in other words, either it will split perfectly in half, or perfectly into a series of equally sized pieces. Little modelling has been done to validate or challenge these assumptions.

This thesis has the following research objectives:

1. Propose a methodology for modelling the fracturing of brittle rock blocks in dynamic settings using a hybrid finite element-discrete element model (FEM/DEM).
2. Investigate geometric relationships related to the fracturing of brittle rock blocks due to gravity free-fall.
3. Investigate the predictive fractal relationships of rock block fragmentation.

### **1.3 Thesis Organization**

This thesis is organized into six chapters including the current chapter and the closing conclusions chapter.

Chapter 2 summarizes a literature review of the main concepts and research used to develop this thesis. It includes information about the theory of brittle rock failure, rock mass strength criteria, methods for estimating block cave fragmentation, and the hybrid finite element-discrete element modelling (FEM/DEM) method.

Chapter 3 describes the development of a FEM/DEM model for modelling rock block breakage due to the gravity free-fall of an intact rock block onto a fixed surface. This section describes the modelling parameters, difficulties encountered with this type of dynamic model, strategies for reducing model instability, and sensitivity of the models to different damping parameters.

Chapter 4 follows from the base case model developed in Chapter 3 and varies the geometric parameters including the rotation of the rock block, the curvature of the hopper surface, and the roughness of the hopper surface. Results are described and interpreted.

Chapter 5 investigates the fractal relationships observed in the models by varying the size of the rock block in the base case model and plotting the results on a log-log plot. In addition, the models described and interpreted in Chapter 4 are plotted on log-log plots to observe possibly predictive fractal relationships in the final block fragmentation.

Chapter 6 provides a summary of the research, key findings and conclusions, limitations and assumptions, and recommendations for future work.

## **Chapter 2: Literature Review**

### **2.1 Introduction**

A literature review of the main concepts and techniques utilized and applied in the development of this thesis is provided in this chapter. Brittle rock failure mechanics is described including basic brittle fracture theory, the two most common constitutive models used to estimate the strength of rock (namely, the Mohr-Coulomb and Hoek-Brown failure criteria), and well as comments on the applicability of these systems to massive or moderately jointed rock masses. Methods for estimating *in situ*, primary, and secondary fragmentation are described including the most common empirical method (Block Cave Fragmentation [BCF] software) and some more recent Discrete Fracture Network (DFN) methods. Lastly, the concept of hybrid finite element/discrete element (FEM/DEM) modelling is discussed.

### **2.2 Brittle Rock Failure**

The failure of rock is determined by the point at which the rock can no longer carry any additional load due to the development of fractures and cracks. The underlying theory of rock fracturing is based on the brittle fracture theory of solids developed by Griffith (1920) which looks at the microscopic development of cracks. Several models have been proposed and applied to rock mechanics that aim to approximate this microscopic behaviour at a macroscopic level including the Mohr-Coulomb failure criterion of materials, and the Hoek-Brown failure criterion of rock. These theories are applicable in many rock engineering problems but recently more research has been conducted that shows the need for a better understanding of the strength of rock masses with little to no natural fracturing at different levels of confinement.

### 2.2.1 Brittle Fracture Theory

The most widely accepted theory of failure of brittle materials is the Griffith theory (1920) which is an energy balance theory that states that cracks in solids will propagate when the reduction in potential energy that occurs due to fracturing is greater than or equal to the increase in surface energy due to the creation of new free surfaces. In other words, if the energy in the solid is sufficient enough to afford the creation of additional surface area, the crack will propagate. These cracks have been shown to occur in the direction of the major principal stress, and cracks naturally not aligned to this stress will propagate along a curved path to align with the major principal stress (Lajtai & Lajtai, 1974)(Figure 2). Eventually, given enough differential stress, fractures will coalesce and the solid can no longer support the change in load (Eberhardt et al., 1998).

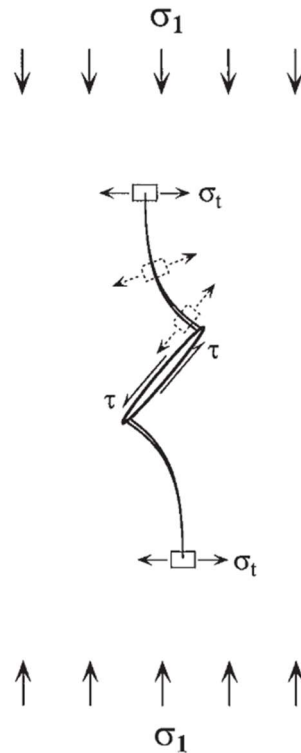


Figure 2: Fracture Propagation in the Direction of Maximum Principal Stress (Eberhardt et al., 1998)

Constitutive models have been developed to simulate this brittle fracture behaviour at the scale of a rock mass while considering the impacts of pre-existing discontinuities and defects. These models include the Mohr-Coulomb (summarized by Labuz & Zang, 2012) and Hoek-Brown (Hoek & Brown, 2019) failure criteria.

### 2.2.2 Mohr-Coulomb Failure Criterion

The Mohr-Coulomb failure criterion provides a description of the conditions for which an isotropic material will fail under differential stress. Labuz & Zang (2012) provide a detailed summary of the failure criterion and the key elements are highlighted in this section.

The criterion is a system of linear equations in principal stress space and can be written as a function of the major and minor principal stresses (i.e.,  $\sigma_1$  and  $\sigma_3$ ) or as a function of normal stress and shear stress (i.e.,  $\sigma$  and  $\tau$ ) on the failure plane. The normal stress is related to the shear stress as shown in Equation 1.

$$\tau = c' + \sigma \tan \varphi' \quad \text{Equation 1}$$

Where  $c'$  represents the effective inherent shear strength or cohesion of the material and  $\varphi'$  represents the effective angle of internal friction. On a plot of shear stress versus normal stress, this equation is represented as a line (Figure 3).

By fitting a circle tangentially to the line (Figure 3), an alternate form of the equation can be written in terms of the principal stresses (Equation 2)

$$(\sigma_1 - \sigma_3) = (\sigma_1 + \sigma_3) \sin \varphi' + 2c' \cos \varphi' \quad \text{Equation 2}$$

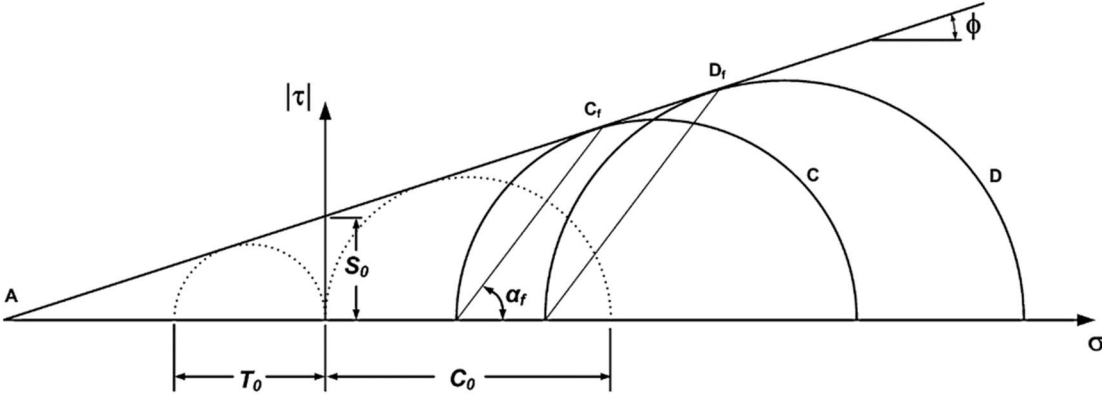


Figure 3: Mohr-Coulomb Failure Criterion (Labuz & Zang, 2012)

### 2.2.3 Hoek-Brown Failure Criterion

The typical approach to estimating the strength of a rock mass utilizes the Hoek-Brown failure criterion (Hoek & Brown, 2019) which relies on the assumption that the failure process of rock masses is predominantly due to movement along open discontinuities in the rock mass. The Hoek-Brown failure criterion is a non-linear failure envelope originally developed in 1980 (Hoek & Brown, 1980a, 1980b) and later updated in 2018 (Hoek & Brown, 2019) and has become the most widely accepted failure criterion for heavily jointed rock masses. The Hoek-Brown equations utilize the Geological Strength Index system (Hoek et al., 2000) to develop input parameters. The generalized equation for the Hoek-Brown failure criterion is shown in Equation 3.

$$\sigma_1 = \sigma_3 + \sigma_{ci} \left( m_b \frac{\sigma_3}{\sigma_{ci}} + s \right)^a \quad \text{Equation 3}$$

$\sigma_1$  and  $\sigma_3$  represent the major and minor principal stresses respectively, while  $\sigma_{ci}$  is the unconfined compressive strength of the intact rock. The variables  $m_b$ ,  $s$ , and  $a$  are material

constants for the rock mass governed by Equation 4 through Equation 6, where D represents the disturbance factor of the rock mass subjected to blast damage and stress relaxation.

$$m_b = m_i \exp\left[\frac{GSI - 100}{28 - 14D}\right] \quad \text{Equation 4}$$

$$s = \exp\left[\frac{GSI - 100}{9 - 3D}\right] \quad \text{Equation 5}$$

$$a = \frac{1}{2} + \frac{1}{6} \left( e^{-\frac{GSI}{15}} - e^{-\frac{20}{3}} \right) \quad \text{Equation 6}$$

For intact rock, the s value is set to 1 and the a value is set to 0.5, which provides a simplified version of the failure criterion.

In many cases, software packages are unable to accept the non-linear Hoek-Brown failure criterion as an input, with preference to linear models such as the Mohr-Coulomb model. In this case, equivalent Mohr-Coulomb parameters can be fit to the Hoek-Brown criterion (Hoek et al., 2002) which balance the area above and below the Mohr-Coulomb curve compared to the Hoek-Brown curve (Figure 4). It is noted that this fit is only applicable to a specific range of rock mass confinement (up to  $\sigma_{3\max}$ ).

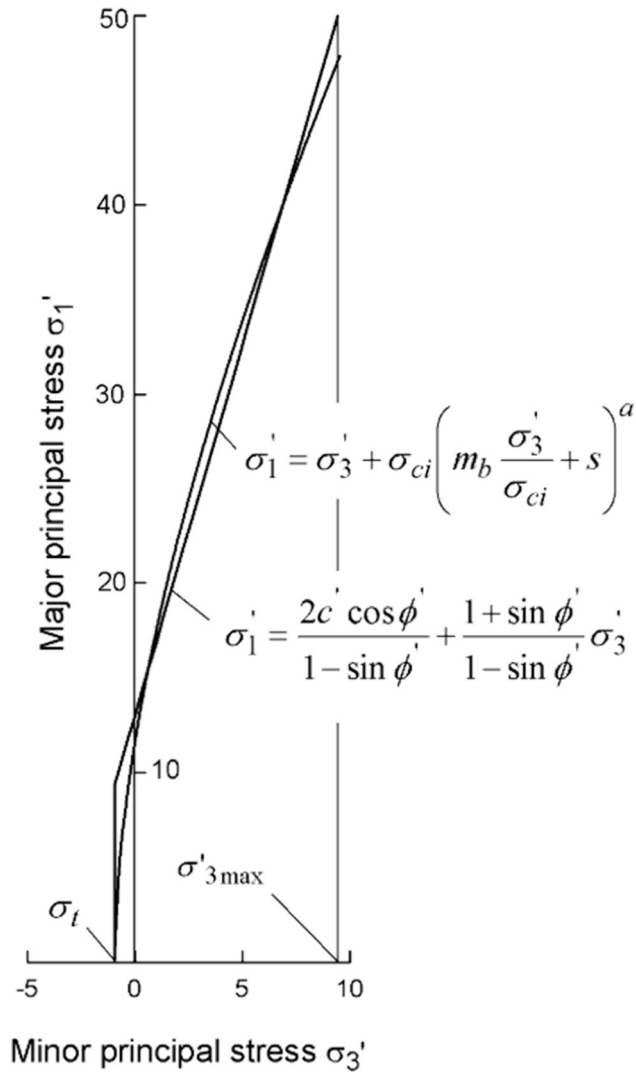


Figure 4: Mohr-Coulomb fit to Hoek-Brown Curve (Hoek et al., 2002)

#### 2.2.4 Rock Fracture in Massive to Moderately Jointed Rockmasses

The GSI system was developed for rock masses that were heavily jointed or blocky and Cai et al. (2004) suggests that Hoek-Brown strengths do not apply to rocks with GSI greater than about 65, namely in rock masses that are massive to moderately jointed. The grey shaded zone in Figure 5 shows the portion of GSI values for which Hoek-Brown parameters are deemed to be not applicable.

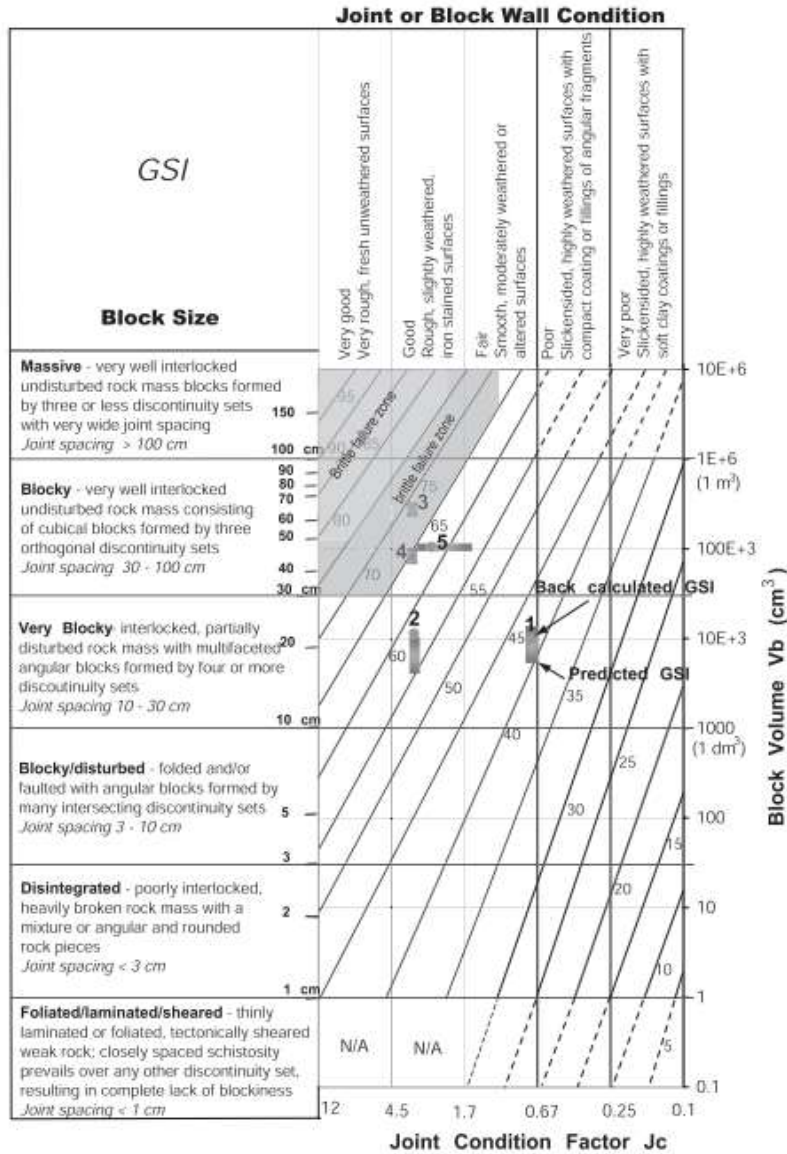
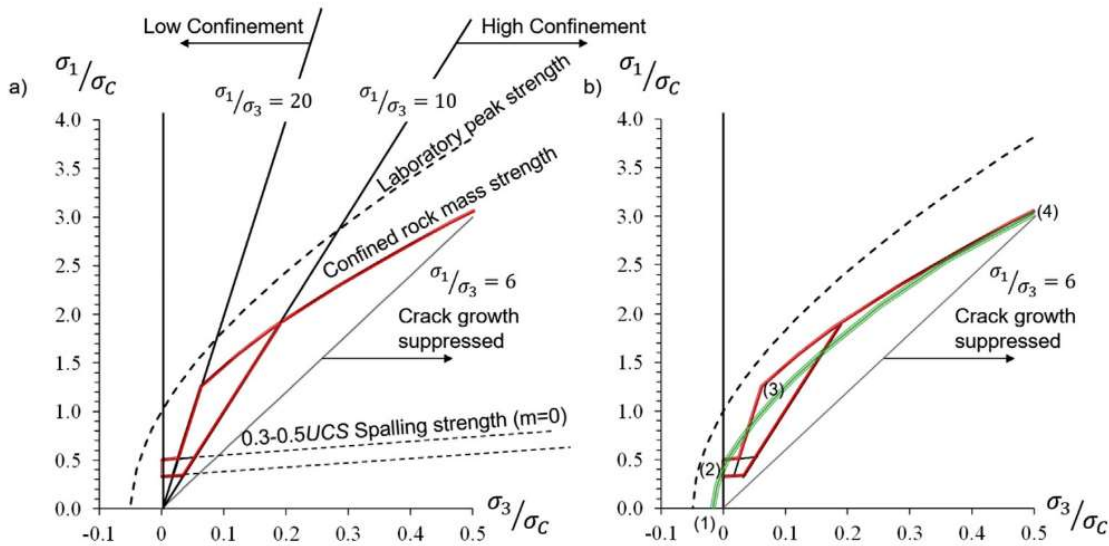


Figure 5: GSI Chart with Grey Shaded Region Showing Rockmasses for which Hoek-Brown Strengths are not Applicable (Cai et al., 2004)

Bewick et al. (2019) propose an alternate strength criterion for massive to moderately jointed rock masses described as a tri-linear curve relevant for the range of confining stresses that could be expected in deep tunnelling and mining (Figure 6). For use in modelling, a Hoek-Brown failure criterion curve can be fit to the tri-linear curve to approximate the strength.



**Figure 6: a) Trilinear Failure envelope (red) relative to Hoek-Brown Failure Criterion and b) Equivalent Non-Linear Fit to the Tri-Linear Envelope (Bewick et al., 2019)**

Failure through intact rock at low confinement near excavation boundaries in massive to moderately jointed rock masses is dominated by extensional (tensional) processes which manifest as thin slabs of rock falling away from the excavation boundary called spalls or spalling. Compressional forces initiate tensile fractures due to local tensile stress concentrations (Diederichs, 1999; Hoek, 1968) and the extent of the tensile fracture propagation depends on the level of confinement, tending to propagate more in low confinement settings and resulting in axial splitting. This zone is represented by the first linear portion of the tri-linear curve at the “spalling strength” which uses the Hoek-Brown equation with  $\sigma_{ci}$  set to 30% to 50% of the unconfined compressive strength and  $m_b$  set to zero. As confinement increases, tensile fractures propagate less and short *en echelon* fractures form and coalesce into shear rupture zones. This zone is represented by the second linear portion of the curve which is defined by a ratio of the major to minor principal stresses which is recommended to be a value between 10 and 20. At

high confinement, the unstable growth of fractures is suppressed, and the strength follows a relationship that resembles a scaled laboratory Hoek-Brown strength curve.

In relation to a block caving secondary fragmentation, the confinement in the ore column is expected to be low compared to the confinement of the rock *in situ*. Therefore, axial splitting will most likely be the dominant failure type with strengths governed by the first portion of the tri-linear curve.

### **2.3 Methods for Estimating Fragmentation**

A variety of methods have been used to estimate the three levels of rock fragmentation in a block cave. Rock mass classification systems such as IRMR, MRMR (D. Laubscher, 2000) and GSI (Hoek et al., 2000) can provide relative estimations of the degree of fracturing in a block cave but are empirically based and tend to be quite general. More numerical solutions have been proposed such as Block Cave Fragmentation (BCF) software (Esterhuizen, 2005) that uses fracture geometry and probabilistic relationships to estimate primary and secondary fragmentation, Core2Frag (Nicholas & Srikant, 2004; Srikant et al., 2004; Wellman et al., 2012) that uses core logging data to estimate the size of *in situ* and primary blocks, and discrete fracture network (DFN) methods that utilize a combination of DFNs with hybrid finite-element/discrete-element (FEM/DEM) modelling to predict *in situ*, primary, and secondary fragmentation (Elmo et al., 2014, 2008; Rogers et al., 2010). The most widely utilized method for estimating fragmentation in the past has been the BCF method, but in more recent years the DFN method has increased in popularity. These two methods are described in detail below.

### **2.3.1 Block Cave Fragmentation (BCF) Software**

The Block Cave Fragmentation (BCF) software was developed to estimate the degree of fragmentation during block caving based on empirical and analytical rules (Esterhuizen, 2005), and has been widely used in the block caving industry (Brobst et al., 2008; Brunton et al., 2016; Jakubec, 2014; Srikant et al., 2004). Since the program is based on empiricism and expert judgement, it contains many assumptions and has a large number of inherent limitations. Due to the widespread use of BCF and the limitations of the program, a review of the methodology of the program is described in the following sections to serve as a baseline of fragmentation estimates. This review focuses mainly on the assumptions the program makes of rock block geometry with less focus on *in situ* and cave stresses. The program contains three modules, one for primary fragmentation, one for secondary fragmentation, and a module for estimating potential hang-ups in drawbells. The primary fragmentation module inherently estimates *in situ* fragmentation, and adjusts this fragmentation based on inputted stress conditions.

#### **2.3.1.1 *In Situ* and Primary Fragmentation from BCF**

BCF (Esterhuizen, 2005) uses the following data to calculate the *in situ* and primary fragmentation:

- Joint data including orientation, spacing, and condition,
- Stress magnitudes,
- Rock mass strength (RMS),
- Intact rock strength (IRS),
- Intact block strength (IBS),
- Mining Rock Mass Rating (MRMR),

- and the Hoek-Brown  $m$  parameter of the rock mass.

Several notes are provided on these required parameters, including some notes that give insight into the limitations of the software. For example, the default joint spacing distribution follows an exponential distribution that is truncated at the minimum and maximum spacing provided by the user. The spacing can also be input as uniform or normal distributions, and the latter assumes the standard deviation is equal to one-third of the range in spacing.

The formation of primary blocks is summarized in the flow chart in Figure 7. Primary blocks are formed by randomly selecting up to six joint surfaces from the joint sets defined, scaled by the defined frequency of each set (Esterhuizen, 2005). The block formation process initiates with the selection of three joints to represent one corner of the block. The first joint is selected with orientation and trace length randomly determined from the input distributions. The frequencies of the remaining sets are modified to remove the initial set, and another joint is selected. Again, the frequencies are modified to remove the second set, and the third joint is selected. These three joints are then intersected to form one corner of the block.

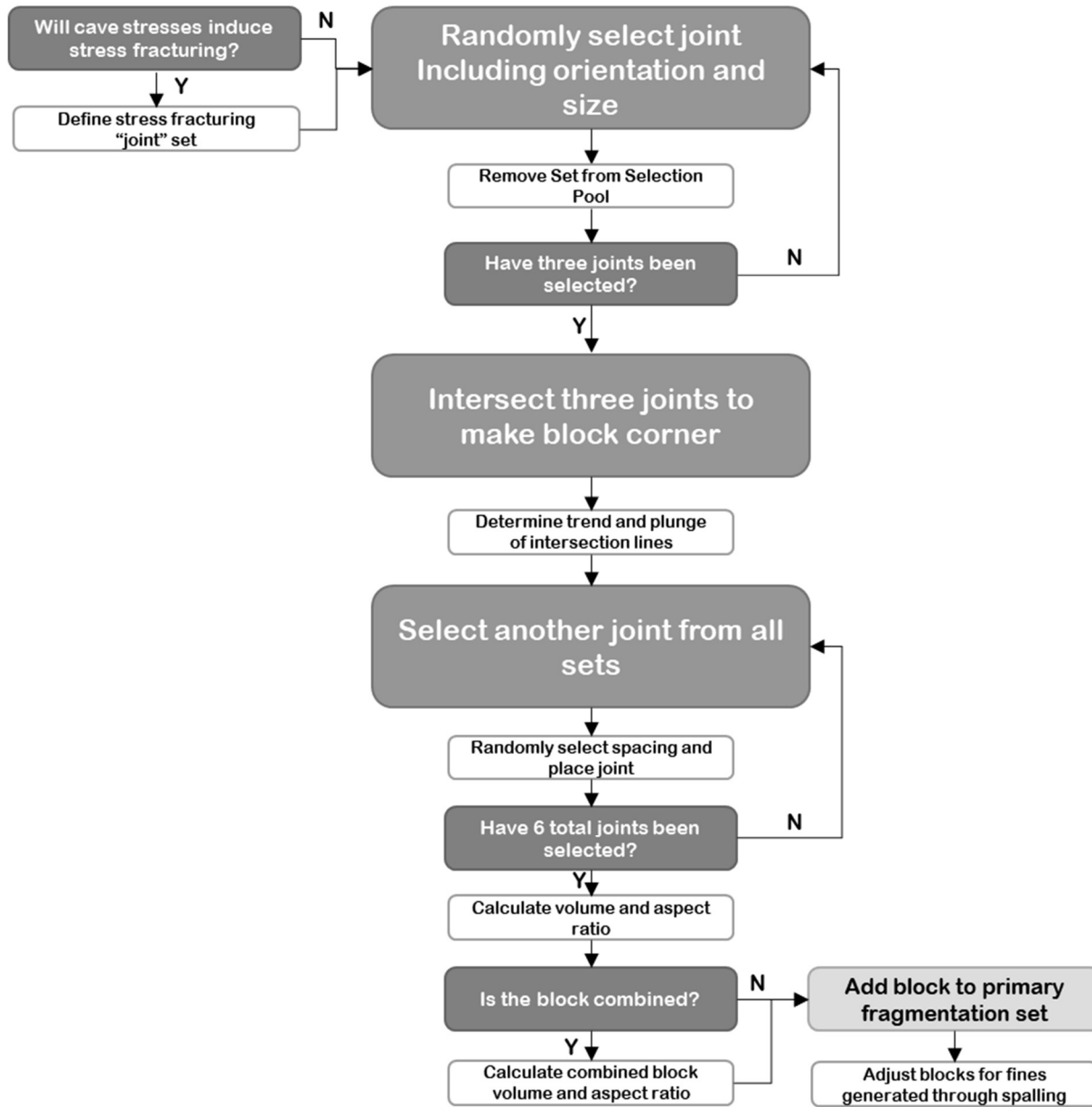


**Figure 7: Flow Chart of BCF Primary Fragmentation Process**

The trend and plunge of intersection lines between the three initial joint sets are determined and, using the frequencies of all the joint sets, a fourth joint is randomly chosen and the distance of the joint along the intersection line is derived from the spacing inputs. This last step is repeated twice to obtain a block defined by six joints. The volume and surface area of the block is

calculated and the aspect ratio ( $\Omega$ ) is calculated as per Equation 7 where V, A and l are the block volume, block surface area, and the length of the longest edge, respectively.

$$\Omega = \frac{A}{6V} l \tag{Equation 7}$$

BCF (Esterhuizen, 2005) also estimates the formation of “combined blocks” which represent two blocks adhered together through joint shear strength. The program considers the joint condition, the stress in the cave back, and the weight of the block to estimate the probability of the formation of a combined block. A schematic of the formation of a combined block is shown in Figure 8.

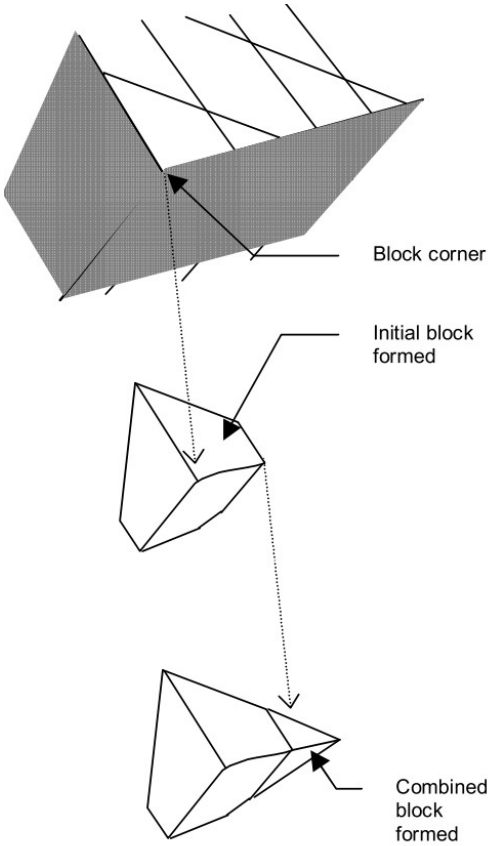
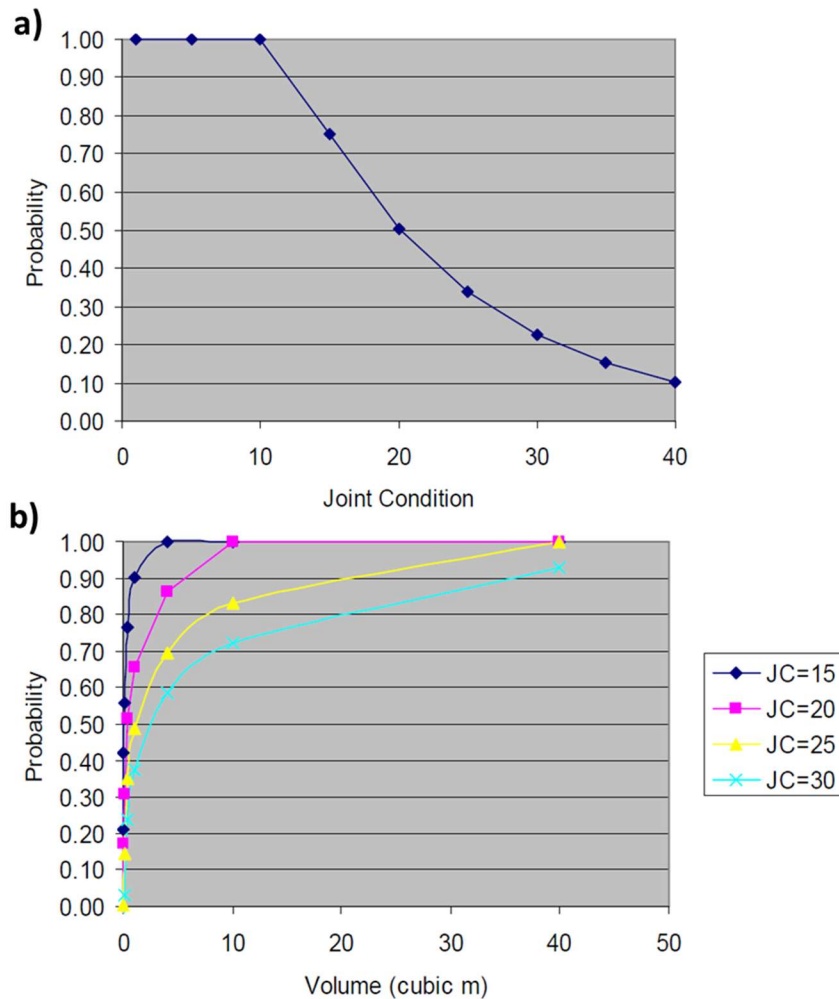


Figure 8: Formation of a Combined Block in BCF (Esterhuizen, 2005).

The joint condition relationship that is used to estimate the probability of separation is shown in Figure 9 (Esterhuizen, 2005). To consider the stress in the cave back, the factor of safety against shearing of the joint is used. This equation assumes a friction angle of 30° and the joint cohesion is determined using Equation 8.

$$C_j = 0.015JC$$

Equation 8



**Figure 9: Probability Relationships Used in BCF Software for a) Joint Condition Probability of Separation and b) Block Weight Probability of Separation (Esterhuizen, 2005)**

Lastly, the relationship that is used to estimate the probability of separation for block weight is also shown in Figure 9 (Esterhuizen, 2005).

The element of primary fragmentation that is considered that differentiates it from *in situ* fragmentation, is stress fracturing. If stresses in the cave back exceed the compressive strength of the rock, and shear failure along joint surfaces does not relieve this stress, intact failure may occur. BCF (Esterhuizen, 2005) uses intact block strength (IBS) to determine the degree of stress fracturing. The factor of safety against failure is determined by comparing the strength to the major principal stress. The IBS is used if at least one of the cave face stresses is set to zero (i.e., biaxial or uniaxial stress), else (i.e., triaxial stress) the Hoek-Brown failure criterion is used to estimate the strength. Stress fractures are always parallel to the cave face with length values between 10 m and 30 m long with an average of 20 m length, by default. Similar to other joint sets, the spacing of stress fractures is assumed to be exponential with a mean based on the factor of safety.

Lastly, spalling can also be considered in the primary fragmentation estimates. Spalling results in the formation of “fines”, however, the program does not consider the stress conditions or strength of the rock when generating these fines, rather a fixed percentage of the rock volume is inputted as “spalled” (Esterhuizen, 2005).

### **2.3.2 Secondary Fragmentation from BCF**

BCF software (Esterhuizen, 2005) also contains a module used to estimate the secondary fragmentation of a block cave. The process for estimating secondary fragmentation is summarized in the flow chart in Figure 10. The module is based on the principle that blocks with high aspect ratios are more prone to splitting than blocks that are equidimensional.

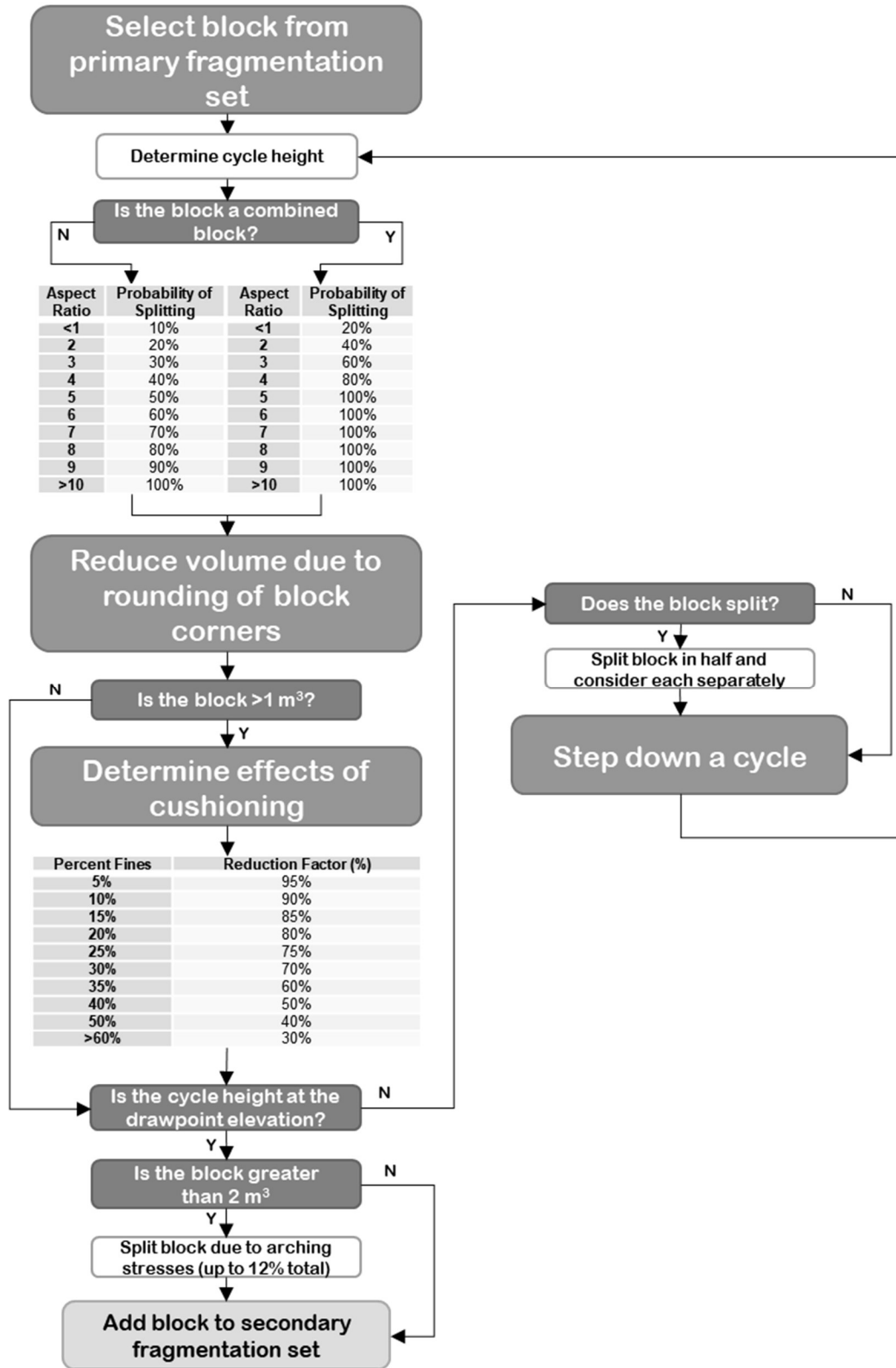


Figure 10: Flow Chart of BCF Secondary Fragmentation Process

The module uses a probabilistic process to split blocks in “cycles” (i.e., the vertical distance that a block with an aspect ratio of 10:1 must travel through the ore column to ensure that it will split). This distance depends on the rock strength and cave pressure. The user specifies a draw height ( $H_d$ ) and the program converts that height to cycles and estimates the secondary fragmentation at that specific draw height. Based on the draw height inputted, the program calculates a caved height ( $H_c$ ). The caved height is defined as the vertical distance that must cave and swell to fill its own volume as well as the drawn volume. It is estimated by a user defined swell factor ( $S_f$ ) (Equation 9).

$$H_c = \frac{H_d}{1 - S_f} \quad \text{Equation 9}$$

The cave height increases until it meets a free surface (such as the ground surface). The caved pressure is calculated by using the weight of the caved material within the caved height based on the density of the rock, the swell factor, and the width to height ratio of the active draw zone, which is defined as the width across the drawpoints which are actively being drawn. As the width of the active draw zone increases the pressure at the base of the ore column increases. A portion of the weight is transferred to the sides of the draw zone based on a relationship between the width to height ratio of the draw zone, with narrower draw zones transferring more weight to the sidewalls than wider draw zones. The proportion of caved weight acting on the base of the ore column is adjusted by the values shown in Table 1. These values have been derived through numerical modelling results (Carranza-Torres, 1998).

**Table 1: BCF Cave Weight Percentage by Active Draw Column Geometry (Based on Esterhuizen, 2005).**

Width to Height Ratio of Active Draw Column	Percentage of Caved Weight Acting on Base of Ore Column
1:1	44%
1:2	30%
1:3	23%
1:4	20%
1:5	18%

The cycle height is determined from the rock block strength (RBS) multiplied by a series of empirical factors. The factors are defined as follows:

- Cycle factor ( $F_c$ ): set to 1 for the BCF program
- Pressure factor ( $F_p$ ): related to the cave pressure, if cave pressure is less than 1 MPa the  $F_p$  is set to 1.  $F_p$  is linearly reduced to 0.5 as pressure increases to 12 MPa. For pressures greater than 12 MPa,  $F_p$  is constant at 0.5.
- Draw rate ( $F_r$ ): a slower draw rate results in rock block remaining in the ore column for longer and therefore reduced block sizes. An empirical exponential relationship has been defined to determine this factor based on the draw rate ( $d$ ) in cm/day (Equation 10).

$$F_r = 0.66 e^{0.023d} \quad \text{Equation 10}$$

The cave pressure is re-calculated for each cycle as the rock block moves down the ore column. The rock block and its products are tracked through each cycle until the drawpoint elevation is reached.

The breakage of the rock in secondary fragmentation determined by BCF is controlled by the following factors:

- aspect ratio,

- rounding of block corners,
- separation of combined blocks,
- cushioning, and
- arching.

The aspect ratio of the primary block is used to determine the probability of splitting (Table 2).

Blocks are always split into two equal-sized blocks. If the probability of splitting dictates that the block is broken, the two products move downwards in the ore column one cycle. This secondary fragmentation process is then repeated for the product blocks. BCF allows a single primary block to produce a maximum of 128 secondary blocks.

**Table 2: BCF Probability of Splitting by Aspect Ratio (Based on Esterhuizen, 2005).**

Aspect Ratio	Probability of Splitting
1	10%
2	20%
3	30%
4	40%
5	50%
6	60%
7	70%
8	80%
9	90%
>10	100%

For blocks containing joints that did not split during primary fragmentation, the probability of block splitting during secondary fragmentation is much higher. A modified probability is applied to the rock blocks with remaining joints based on the aspect ratio as shown in Table 3.

**Table 3: BCF Probability of Splitting of Combined Blocks by Aspect Ratio (Based on Esterhuizen, 2005).**

Aspect Ratio	Probability of Splitting
1	20%
2	40%
3	60%
4	80%
5	100%
6	100%
7	100%
8	100%
9	100%
>10	100%

The process above is adjusted by the effects of rounding of block corners resulting in the production of “fines”. The amount of fines depends on the acuteness of the corners of the blocks which is determined by the variation in joint orientations for the corner, shown in Equation 11 where  $\mu$  represents the variation between joint set orientation angles in degrees.

$$V_r = 3 + \frac{\mu}{5} (\%) \quad \text{Equation 11}$$

This percentage is calculated for the initial block and every time a block splits and the proportion calculated is removed from the block volume and converted to fines.

When fines prevent contact between large rock blocks and therefore reduce the induced stresses and fragmentation potential, the effect is called cushioning. Only fines generated during primary fragmentation are considered active in cushioning in the BCF software and only blocks with volumes greater than 1 m<sup>3</sup> are affected by cushioning in the program. A reduction factor on the block splitting probability is applied based on the percentage of fines (Table 4).

**Table 4: BCF Cushioning Adjustment by Percentage of Fines (Based on Esterhuizen, 2005).**

Percent Fines	Reduction Factor (%)
5%	95%
10%	90%
15%	85%
20%	80%
25%	75%
30%	70%
35%	60%
40%	50%
50%	40%
>60%	30%

Lastly, the program considers arching effects in secondary fragmentation. When blocks get caught into temporary arches, they will only be free when one of the blocks breaks from induced stresses. Arching stresses are assumed to be a function of the cave pressure. The program uses a default concentration factor of 25 times the cave pressure for arching stress. It is assumed that a maximum of 12% of the blocks split as a result of the arch formation and that it only affects blocks greater than 2 m<sup>3</sup>. When a block reaches the drawpoint elevation, blocks greater than 2 m<sup>3</sup> are randomly selected to be split (up to a maximum of 12% of blocks) if cave pressures dictate.

### **2.3.3 Discrete Fracture Network (DFN) Models**

In recent years, discrete fracture network (DFN) modelling has become increasingly popular for estimating the distribution of block cave fragmentation (Elmo et al., 2014, 2008; Rogers et al., 2010). DFNs are created by stochastically generating the intensity, orientation, persistence, and location of fractures within a model area using probability density functions defined from collected data (Dershowitz et al., 1998; Elmo et al., 2008). DFN methods have a series of

advantages including the ability to capture heterogeneity in rock masses as well as accurately describing local-scale fractures compared to large-scale continuum methods. This approach utilizes a variety of data sources such as data from mapped outcrops and data logged from boreholes. Of particular interest to the DFN modeller is the fracture intensity, as this parameter is usually estimated with empirical rock mass classification schemes in continuum-based methods. Intensity can typically be estimated from fracture samples collected from core logging or outcrop mapping. An intensity naming scheme has been developed to remove ambiguity when discussing fracture intensity called the  $P_{ij}$  system (Figure 11). The  $P_{ij}$  system defines fracture intensities based on the dimensions of the sample ( $j$ ) and the dimensions of the measurement ( $i$ ). For example, fracture frequency measured from a one-dimensional borehole (i.e., count of fractures per length of the borehole) has a sample dimension of 1 (length) and a measurement dimension of 0 (count), therefore this intensity measurement would be called  $P_{10}$  (Dershowitz et al., 1998).

		Dimension of Measurement			
		0 	1 	2 	3 
Dimension of Sample	1 	<b>P10</b> No of fractures per unit length	<b>P11</b> Length of fracture per unit length		
	2 	<b>P20</b> No of fractures per unit area	<b>P21</b> Length of fracture per unit area	<b>P22</b> Area of fracture per unit area	
	3 	<b>P30</b> No of fracture per unit volume		<b>P32</b> Area of fractures per unit volume	<b>P33</b> Volume of fractures per unit volume
		<b>Density</b>		<b>Intensity</b>	<b>Porosity</b>

Figure 11: FracMan  $P_{ij}$  intensity classification scheme (based on Dershowitz et al., 1998)

Preferably, the volumetric fracture intensity ( $P_{32}$ ) is used for the development of a DFN model as a sample of fractures per volume is theoretically directionally unbiased; However, this property is difficult, if not impossible, to directly measure. Typically,  $P_{32}$  is linearly related to  $P_{10}$  and a relationship can be found to convert borehole intensities to volumetric intensities. Several analytical solutions exist to convert  $P_{10}$  values into  $P_{32}$  values (Chiles et al., 2008; Wang, 2005).

### 2.3.3.1 *In Situ* Fragmentation from DFN Models

DFN models allow the prediction of *in situ* rock block size in a block cave (i.e., *in situ* fragmentation). To do this, a DFN model is stochastically generated in a large volume and sampled with a smaller sub-volume (Rogers et al., 2010). The larger volume is used to avoid potential edge effects of the DFN fracture generation and ultimately the size of these regions depends on the cave volume and resolution of the data collected. The external boundaries of the

sub-volume are considered to be fractures and this assumption allows for mass balance between the iterations. Blocks are determined by using the Sybil Frac algorithm as shown in Figure 12 (Dershowitz et al., 1998). This algorithm overlays a fine grid of cells onto the DFN, fractures are then mapped into this grid at approximate grid boundaries and blocks are then assembled by connecting grid cells not separated by fractures. This procedure depends on the size of the grid cells used and it is suggested that grid cells not larger than 25% of the fracture spacing be used (Elmo et al., 2014).

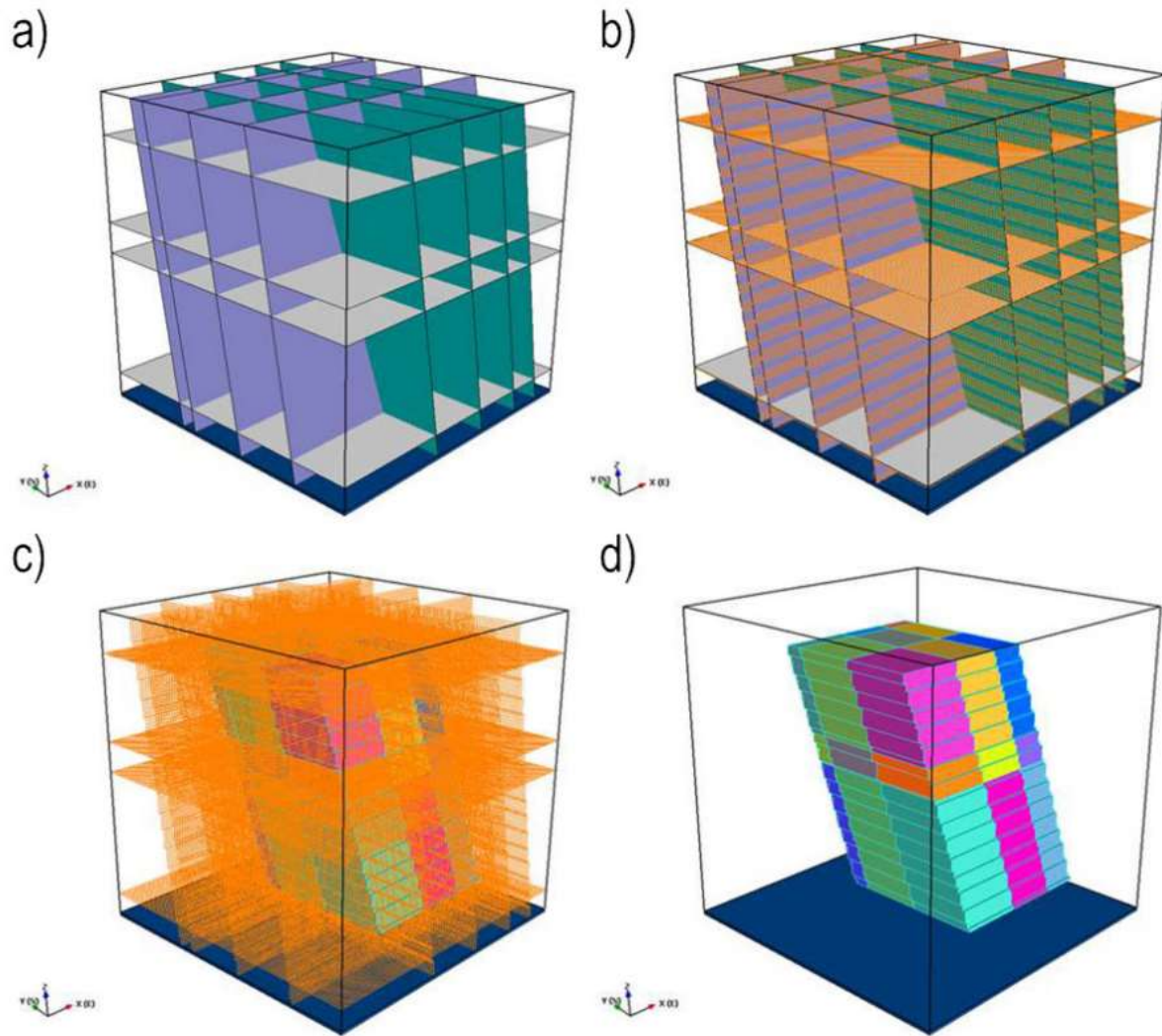


**Figure 12: Example of the Sybil Frac Algorithm used on a DFN Model showing a) The Initial DFN b) The Fractures Mapped onto the specified grid c) blocks mapped into the grid and d) the final block blocks formed (Elmo et al., 2014)**

Rogers et al. (2010) suggest an efficient solution to determining the *in situ* fragmentation. First, the P32 of each cave lift and domain within that lift is determined. Block size models for a variety of P32 values are generated based on the distribution of P32 values within the domain volume. Block size calculations are conducted for several iterations on each of these models. The

resulting size distribution curves are then weighted based on the original P32 distributions for each lift and domain to produce a representative block size curve.

### 2.3.3.2 Primary Fragmentation from DFN Models

To estimate primary fragmentation, a combined approach using both DFN modelling and FEM/DEM modelling has been suggested as an alternative to BCF (Rogers et al., 2010). The details of FEM/DEM modelling are described later in Section 2.4; however, the FEM/DEM code ELFEN (Rockfield, 2011) was utilized to estimate the amount of induced fracturing due to stresses developed during cave evolution on a series of two-dimensional sections sampled and plane-strain filtered from the *in situ* DFN models (Elmo et al., 2010; Rogers et al., 2010). Stress fracturing results of models of the 10<sup>th</sup>, 50<sup>th</sup>, and 90<sup>th</sup> percentiles of P32 intensity of a DFN model are shown in Figure 13.

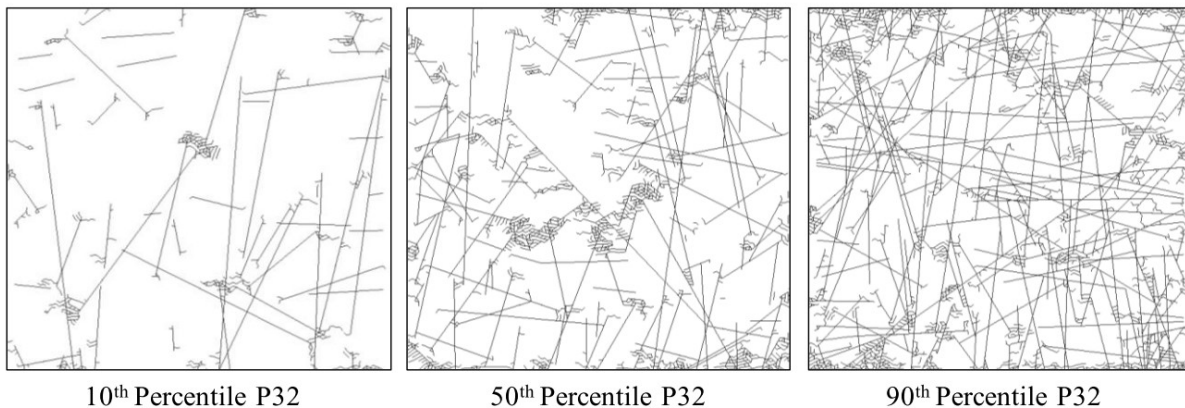


**Figure 13: Results of the FEM/DEM Modelling of Primary Fragmentation for the 10<sup>th</sup>, 50<sup>th</sup>, and 90<sup>th</sup> Percentile of P32 Intensity (Rogers et al., 2010)**

The modelling shows a tendency for fractures to generate sub-parallel to the maximum horizontal stress, with size described by an exponential distribution. The intensity was noted to

be related to the *in situ* intensity by a conversion factor with fractures more likely to develop in areas of higher fracturing (i.e., at intersections of *in situ* fractures).

Based on the ELFEN simulations the properties of induced stress fracturing were quantified and simulated in the DFN models and the Sybil Frac algorithm was again utilized to estimate block size distributions.

### **2.3.3.3 Secondary Fragmentation from DFN Models**

For secondary fragmentation, the DFN method utilizes a rule-based probabilistic approach similar to BCF, however, informed by DFN and FEM/DEM modelling (Rogers et al., 2010).

Primary fragmentation is assumed to be largely controlled by the presence of micro-defects or veins, therefore, these features are explicitly modelled on small-scale block size DFN models to estimate the resulting block size using the Sybil Frac algorithm. These models were completed for a series of block sizes and defect intensities to obtain relationships that can be used in a probabilistic model.

Block breakage is assumed to be affected by differences in draw height; therefore, FEM/DEM models were used to estimate a relationship between breakage efficiency and effective cave stresses on the block. These models applied variable loading conditions to a collection of rock blocks with different defect intensities (Figure 14).

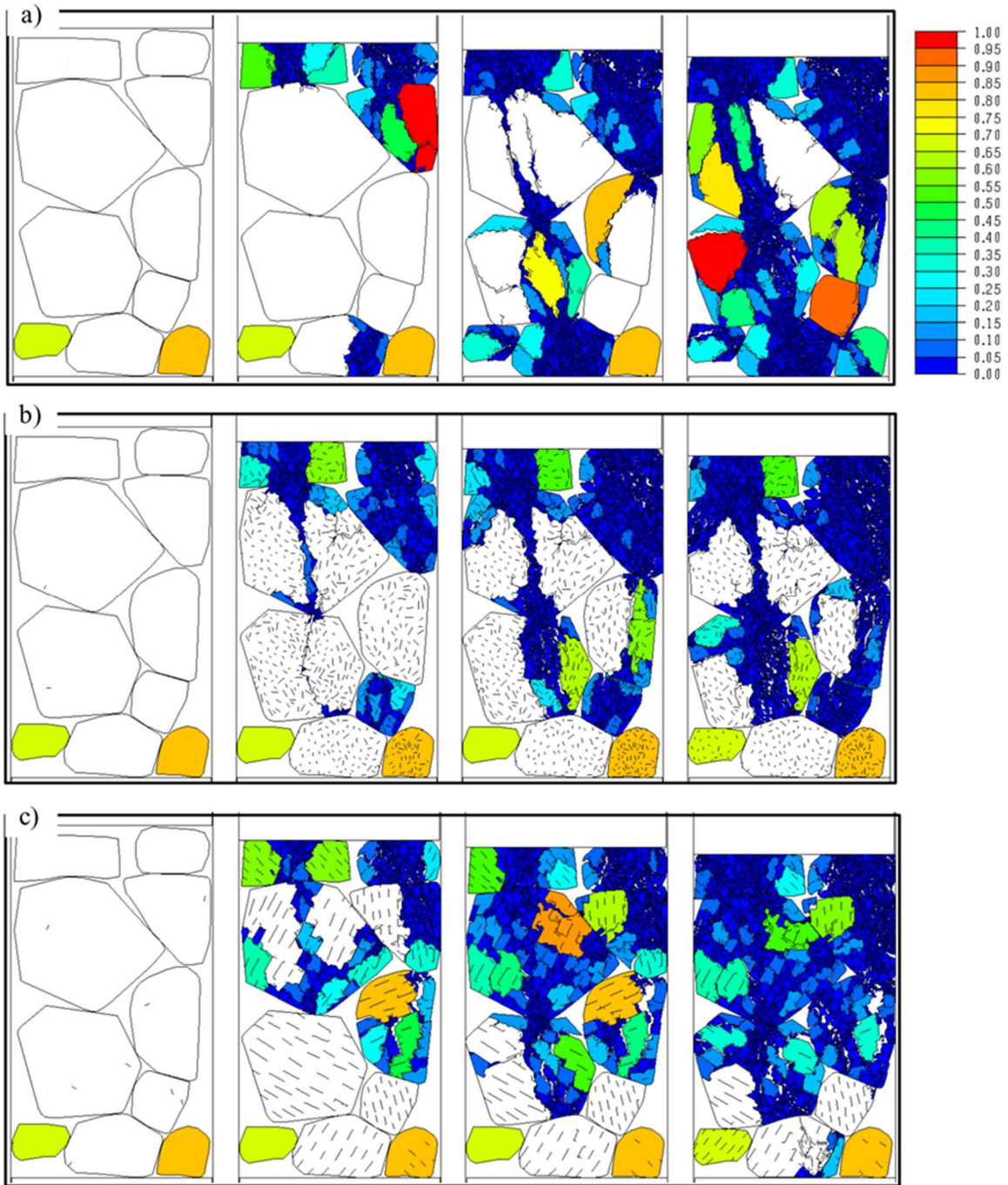


**Figure 14: FEM/DEM Modelling of Rock Blocks within a Cave with Different Defect Intensities a) Intact Blocks b) Blocks with Randomly Oriented Defects, and c) Blocks with Defects at a Constant Orientation (Rogers et al., 2010)**

Using the relationships developed in DFN and FEM/DEM modelling, a probabilistic model was run utilizing the following steps (Rogers et al., 2010):

- Randomly select a block size from the primary fragmentation distribution,
- Randomly select a defect intensity based on the input for each lift and domain,
- Based on the defect intensity, determine the percentage of the block that can possibly form secondary blocks using relationships developed from DFN modelling.
- Randomly draw a value of breakage efficiency from the relationship developed from FEM/DEM modelling to determine how much of the secondary block volume will actually form.
- Estimate the mean block size volume based on the defect intensity and DFN modelling and split the efficiency-scaled block forming percentage of the primary block into sub-blocks with equal volumes.

This process is repeated thousands of times to obtain a representative secondary block size distribution.

## **2.4 Hybrid Finite Element/Discrete Element Modelling**

Hybrid FEM/DEM analysis has been extensively used to simulate a variety of rock engineering problems (Elmo et al., 2013), including laboratory strength tests (Cai & Kaiser, 2004; Elmo et al., 2011; Hamdi et al., 2015; Karami & Stead, 2008), failure of hard rock pillars (Elmo & Stead, 2010), brittle failure of rock slopes (Eberhardt et al., 2004; Stead et al., 2006; Yan, 2008), and block cave development and subsidence analysis (Vyazmensky, 2008; Vyazmensky, Elmo, et al., 2010; Vyazmensky, Stead, et al., 2010). FEM/DEM models use a combination continuum and discontinuum; deformation of discrete elements is determined by continuum mechanics while the

interaction and motion of the discrete elements are determined by discontinuum mechanics (Munjiza, 2004). In other words, each body is represented by a single discrete element that can interact with other discrete elements, and within each discrete element is a finite element mesh that is used to model the deformation of the body. The transition from a continuum to discontinuum is determined through fracture mechanics constitutive models which split single discrete elements into multiple discrete elements each with a respective finite element mesh. There are many hybrid FEM/DEM codes available, for this study ELFEN (Rockfield, 2011) was utilized. It includes a coupled, elastoplastic fracture-mechanics criteria that models the continuum/discontinuum transition realistically.

#### **2.4.1 ELFEN Input Parameters**

There are two main types of input parameters required in the ELFEN code: material strength parameters which govern the stress/strain response of the discrete bodies, and contact parameters which govern the interaction between the discrete bodies.

##### **2.4.1.1 Material Strength Parameters**

ELFEN incorporates the elastic properties of the materials including Young's Modulus ( $E$ ) and Poisson's Ratio ( $\nu$ ) to estimate the stress and strain properties. To estimate the ultimate strength of the rock, ELFEN performs best using a Mohr-Coulomb failure criterion rather than a Hoek-Brown failure criterion, so this constitutive model was used for FEM/DEM model development coupled with a Rankine rotating crack tensile cutoff. The Mohr-Coulomb criterion is limited in its ability to represent failure in tension and the Rankine rotating crack tensile cutoff is used to overcome this limitation. The model is described in mathematical detail by others (Klerck, 2000;

Klerck et al., 2004), but a brief overview is provided here. The Rankine model creates a Mode I (extensional) crack in the mesh when any principal stress ( $\sigma_1, \sigma_2, \sigma_3$ ) reaches the tensile strength of the rock ( $\sigma_t$ ) (Equation 12).

$$\sigma_i - \sigma_t = 0 \quad \{i = 1, 2, 3\} \quad \text{Equation 12}$$

When a crack in the mesh is introduced, it is oriented such that the crack propagates in the direction of the major principal stress (i.e., the normal to the crack is aligned with  $\sigma_3$ ). The propagation of the crack is controlled in ELFEN by relating the length of the fracture and the fracture energy to derive a stress intensity factor which degrades the elastic modulus in the direction of the major principal stress invariant which is then checked against the failure criterion in the next loading step (Cai & Kaiser, 2004; Elmo et al., 2013; Munjiza, 2004).

Both the formation and propagation of cracks within the finite element mesh are limited by the mesh topology. Two options exist for the insertion of new fractures into the mesh: intra-element fracturing or inter-element fracturing (Klerck et al., 2004) (Figure 15). Intra-element fracturing inserts a new fracture at the orientation and location governed by the Rankine rotating crack model. The element is then re-meshed to include this fracture. Inter-element fracturing creates fractures along existing mesh boundaries closest to the orientation determined from the Rankine

rotating crack model.

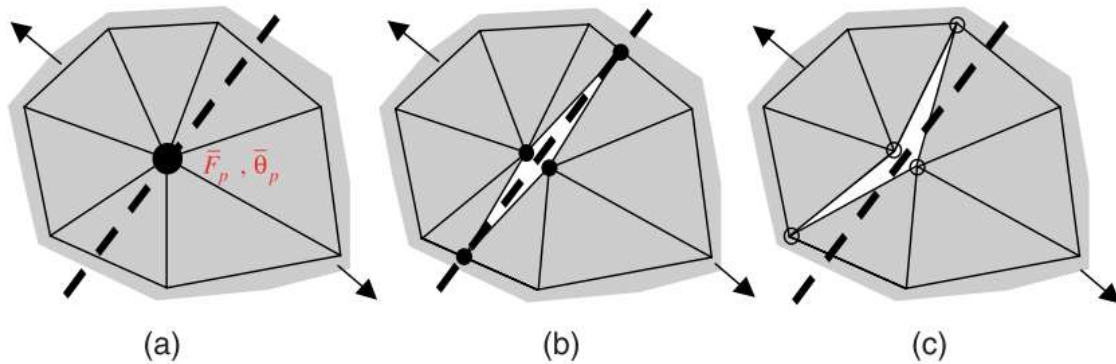


**Figure 15: a) Fracture Plane Direction from the Rankine Rotating Crack Model, b) Intra-element Fracturing and c) Inter-element Fracturing (Klerck et al., 2004).**

Each method of fracture insertion has advantages and disadvantages, however, typically, intra-element fracturing is preferred. Intra-element fracturing has the advantage of accurately reproducing the fracturing directions, however, it is disadvantageous due to the possibility of highly irregular meshes that can be computationally expensive due to the need to update the mesh topology after the introduction of each fracture. The updated topology can result in model instability due to irregular meshing. Inter-element fracturing has the advantage of not requiring the regeneration of mesh topology after each fracture insertion which leads to shorter computational times and, in turn, more stable models; however, it is disadvantageous because the fracturing is highly dependent on the mesh orientation, meaning it may require smaller meshes to achieve reasonable fracturing simulation.

#### **2.4.1.2 Contact Parameters**

In addition to the finite element properties included in the model, contact properties must also be specified. In this case, the Mohr-Coulomb strength criterion can also be applied to the frictional

resistance of the discrete elements contacts which get applied to initial model contact boundaries as well as any new fractures generated through the modelling process. In addition to the frictional parameters, contact penalties are also required. These penalties (both normal and tangential) are used to govern the simulation of discrete element interaction by reducing the amount of element penetration (Klerck, 2000; Munjiza, 2004). When two bodies contact each other, they are assumed to penetrate which results in contact force which is governed by the penalty inputs. Typically, the normal penalty is defined in the range of half of the Young's modulus to double the Young's modulus of the material and the tangential penalty is typically 10% of the normal penalty (Rockfield, 2011).

Lastly, the code requires two parameters that determine whether or not bodies are in contact: the contact field and the search zone. The contact field parameter is typically chosen at 10-20% of the side length of the mesh (Rockfield, 2011) and represents the thickness of the contact layer corresponding to the maximum permissible penetration. In other words, when one body is within the contact field of another body, the contact penalties will be applied. The search zone parameter is typically chosen to be equal to the side length of the mesh elements (Rockfield, 2011) and represents the size of the buffer zone that will be used to search for contacts. In other words, this parameter is used to determine which bodies will come into contact and will need to have contact forces computed. Figure 16 shows a schematic of these two parameters.

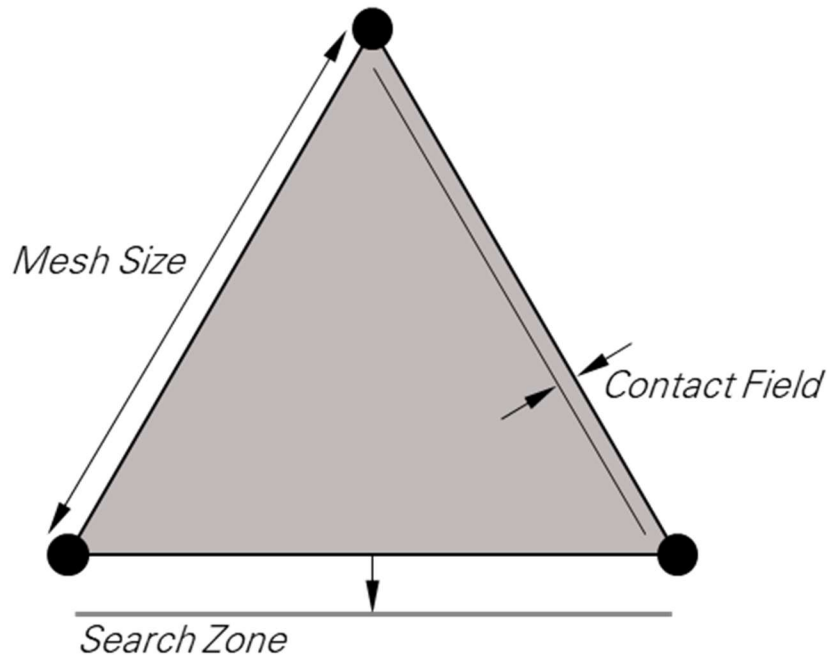


**Figure 16: Schematic of Contact Field and Search Zone FEM/DEM Parameters (Not to Scale).**

## 2.5 Chapter Summary

Brittle rock failure is the fundamental concept behind block cave fragmentation and rock mass strength constitutive models are used to simulate this failure. There are several different models available for estimating rock block strength each with increasing levels of complexity.

Many methods have been used to estimate block cave fragmentation, the most popular being the BCF program and the DFN method. BCF uses a series of assumptions and formulae based on empirical methods and rock strength criteria to determine the *in situ*, primary, and secondary fragmentation and is subject to limitations resulting from some of the more simplistic assumptions. For example, BCF assumes that when a rock block splits, it will split perfectly in half, which is a major assumption and limitation of this software. The DFN method attempts to provide more control over the fracture inputs and development to obtain better rock block size

distributions by using probabilistic distributions to model the discrete discontinuities within the rock mass but is still subject to limitations. Similar to BCF, the DFN method assumes that when a block splits, it will split into equally sized sub-blocks, which is also a major assumption and a limitation of this method.

FEM/DEM models have been used to model a variety of different rock engineering problems. A series of parameters are required for FEM/DEM models that govern the movement, deformation, and transition from continuum to discontinuum of discrete bodies. The choice of parameters can greatly affect model stability and model run times and should be considered carefully when developing FEM/DEM models.

## **Chapter 3: Hybrid Finite Element/Discrete Element Model Development**

In order to estimate the fragmentation of brittle rock blocks, a gravity free-fall hybrid finite element/discrete element (FEM/DEM) model was developed consisting of a fixed hopper a singular square rock block falling due to gravity. This simple model is used to understand how a rock block may fracture and is most applicable to the stage of block caving where a rock block falls from the back of the cave and travels through the air gap in towards the ore column but can be extrapolated to understand how a rock block may fragment under unconfined conditions. The goal of the modelling process was to develop a model that is practical for engineering purposes, in other words, a desirable model would produce useful results in a reasonable time frame. The model described below has computation times between four to six hours, rather than some FEM/DEM models which can typically take 12 or more hours to compute.

### **3.1 Base Case Model Development**

The base case model geometry is shown in Figure 17. The hopper has a 10 m by 10 m internal area and the rock block has a 3 m by 3 m area. A uniform triangular finite element mesh was applied with a target side length of 0.1 m. Meaning the smallest equilateral triangle formed has an area of approximately  $4.3e-3 \text{ m}^2$ . The models were not permitted to fracture below the minimum mesh size; further discussion on the impacts of this are included below. Only the rock block was permitted to fracture, and the hopper was modelled as a finite element continuum. The hopper was fixed in the x and y directions and a global gravity value of  $-9.81 \text{ m/s}^2$  was applied to the system to simulate the free-fall of the rock block.

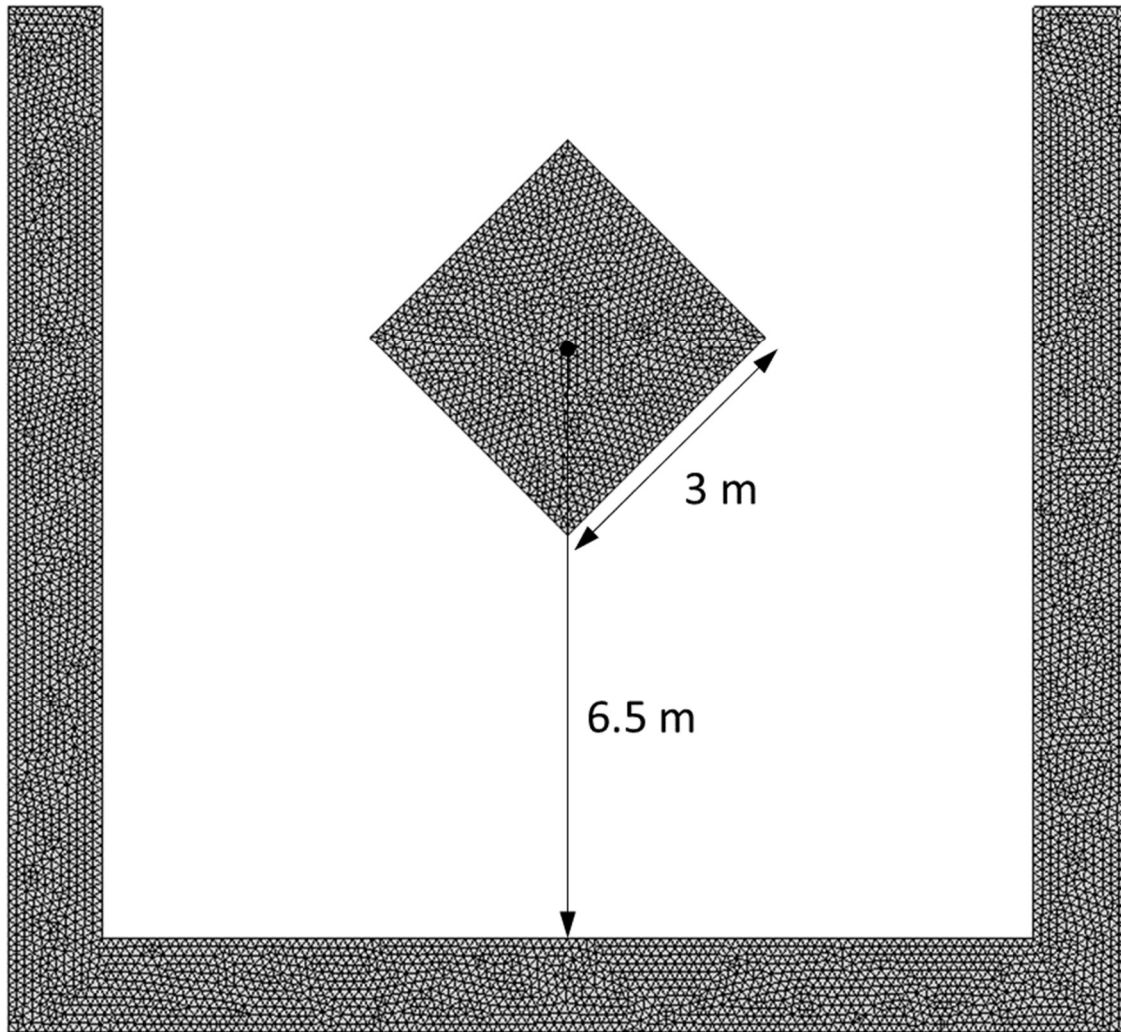


**Figure 17: FEM/DEM Base Case Model Geometry Showing Rock Block, Hopper, and Triangular Mesh.**

Several iterations of the base case model were tested before arriving at a model that met the modelling goals. In early iterations of the model, the rock block was initially placed such that the bottom edge of the block, when parallel to the hopper base, was 5 m above the base of the hopper and the centroid of the block was 6.5 m above the base of the hopper. When the rock block was dropped with the base parallel to the hopper, the full line-to-line contact of the block tended to cause model instability due to the instantaneous energy transfer seen at the initial point

of contact. Therefore, for the base case model, the rock block was rotated 45 degrees such that the point of the block was the first to contact the hopper during gravity free-fall, to allow for simpler testing of modelling parameters. Subsequent modelling tested the impact of the point-contact versus line-contact of the rock block and hopper. Similarly, early models allowed intra-element fracturing, however, long model run-times and high degrees of model instability made this an impractical, if not impossible, choice due to the highly dynamic nature of this simulation and the limitations of ELFEN software.

The constitutive model used for the strength estimation of the rock block, as mentioned in Section 2.4.1.1, was the Mohr-Coulomb strength model coupled with the Rankine Rotating Crack fracture model with a tensile cutoff (Klerck, 2000; Klerck et al., 2004).

The material parameters in Table 5 were used for the rock block, hopper and contacts in the model. The modelled rock material represents a strong, brittle rock typical of the altered granitic rock which may be seen in many copper-porphyry deposits.

**Table 5: FEM/DEM Model Material Parameters.**

Material	Parameter	Value	Unit
Rock	Elastic Modulus (E)	49	GPa
	Poisson's Ratio ( $\nu$ )	0.21	-
	Density ( $\rho$ )	2,700	kg/m <sup>3</sup>
	Cohesion (c)	19.8	MPa
	Friction Angle ( $\phi$ )	53	°
	Dilatancy Angle ( $\phi$ )	5	°
	Tensile Strength ( $\sigma_t$ )	8.4	MPa
	Fracture Energy ( $G_f$ )	30.4	J/m <sup>2</sup>
Hopper	Elastic Modulus (E)	17.80	GPa
	Poisson's Ratio ( $\nu$ )	0.21	-
	Density ( $\rho$ )	2700	kg/m <sup>3</sup>
Contacts	Normal Contact Penalty	49	GPa
	Tangential Contact Penalty	4.9	GPa
	Friction Angle ( $\phi$ )	31	°

Fracture energy was estimated using the formula shown in Equation 13.

$$G_f = \frac{K^2}{E} \quad \text{Equation 13}$$

Where  $G_f$  is the fracture energy,  $K$  is the fracture toughness, and  $E$  is the elastic modulus of the rock assuming plane stress conditions. Fracture toughness ( $K$ ) was estimated using the empirical relationship described by Zhang (Zhang, 2002) and shown in Equation 14.

$$\sigma_t = 6.88K \quad \text{Equation 14}$$

Where  $\sigma_t$  is the rock tensile strength.

Additionally, the modelling parameters in Table 6 were used in the FEM/DEM model.

**Table 6: FEM/DEM Modelling Parameters**

Parameter	Value	Unit
Global Contact Damping	0.3	-
Top Frequency Damping	2	-
Rigid Body Motion Damping	2	-
Contact Field	0.07	m
Search Zone	0.15	m
Factor of Critical Time Step	0.1	-

Determination of these parameters stemmed from similar FEM/DEM models developed by others (Elmo et al., 2013, 2010; Vyazmensky, Stead, et al., 2010) as well as guidance on typical values provided by Rockfield and Munjiza (Munjiza, 2004; Rockfield, 2011). The damping parameters will be discussed in more detail in the model sensitivity section.

In this case, a larger contact field was chosen than what is typically used in FEM/DEM models (typically equal to 10-20% of the side length). Due to the high velocities in this model, elements can exceed the contact field within a singular timestep and therefore contact penalties may be fully applied nearly instantaneously, resulting in extremely high stresses over a short period, which led to model instability. Increases in the contact field allow for elements to have contact stresses applied gradually, at expense of model computation time.

Similarly, in this case, a slightly larger search zone (typically equal to the target side length) was used at the expense of computational efficiency for the same reason as the contact field. High velocity elements may not be detected as being in contact with other elements between timesteps, resulting in large penetrations and subsequent instantaneous contact penalties. Increases in the search zone allow for element contact detection over several timesteps for high velocity elements.

The factor of critical timestep is used to determine which timestep to utilize for model runs. The critical timestep is calculated using Equation 15, where  $l$  is the smallest side length, and  $c$  is the wave speed. The wave speed is approximately the square root of the ratio between the Young's Modulus and the density of the material.

$$\Delta t_{cr} = \frac{l}{c} \quad \text{Equation 15}$$

The timestep used in the model is the critical timestep multiplied by the factor of critical timestep.

Since elements cannot fracture smaller than the mesh size, the energy that would be absorbed through the fracturing process needs to be expressed as another form of energy. In other words, this energy is either damped, converted to kinetic energy, or converted to elastic energy. When the would-be fracturing energy is converted to kinetic energy, elements tend to exhibit considerably large velocities. Similarly, when converted to elastic energy, the elements tend to exhibit high degrees of deformation. In many cases, both high velocity and high deformation are seen in small elements as shown in Figure 18. These high degrees of deformation and high velocities often result in model instability and unrealistic rock block fracturing.

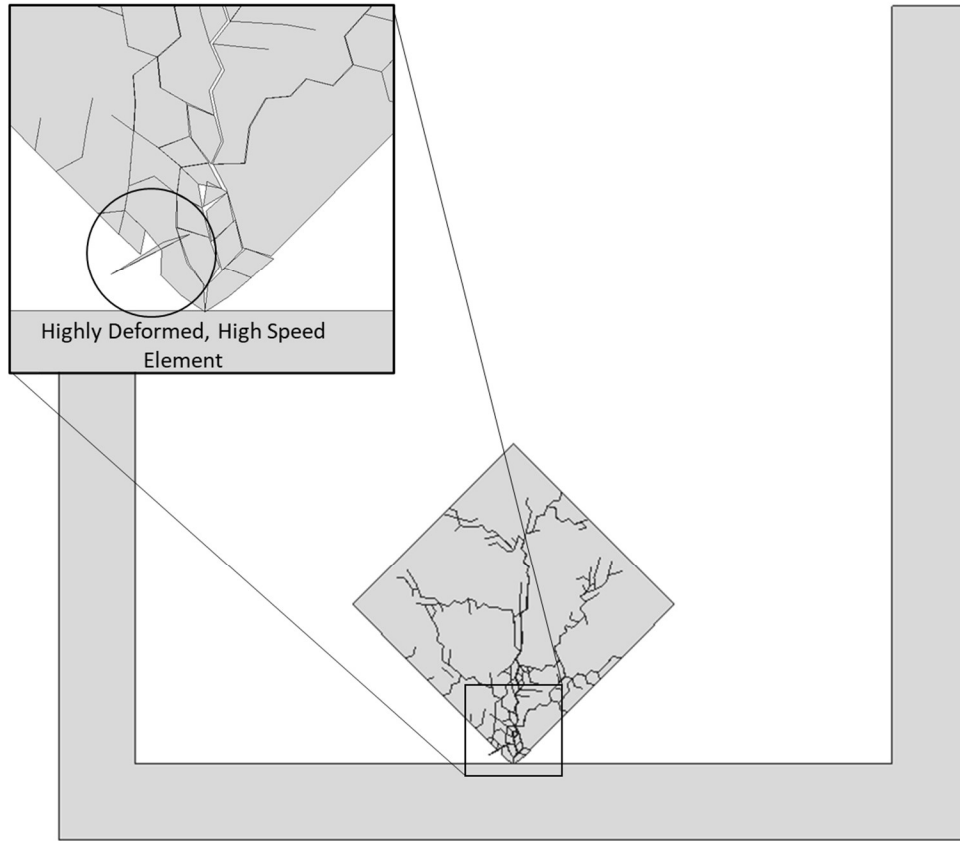


**Figure 18: ELFEN Model without Deletion Sequence Showing Highly Deformed, High Speed Modelling Artefact.**

The high deformations and velocities are considered modelling artifacts and not representative of reality, therefore, a deletion sequence was added to the model that removes elements with velocities greater than 20 m/s and elements with critical timesteps less than  $1e-10$  seconds. The critical time step is determined by the ratio between the length of the smallest element and the wave speed. Therefore, when the length of an element becomes considerably small, the critical timestep becomes very small, therefore, this measure is a good proxy for element deformation. The threshold values for these parameters are somewhat arbitrary, however, the velocities of the kinetic energy artifacts are orders of magnitude higher than the threshold and the timesteps of the

elastic energy artifacts are orders of magnitude lower than the threshold. The values chosen do not appear to affect the model fragmentation unrealistically; however, further study is warranted on the effect that these parameters have on final fragmentation. The elements that are removed are assumed to fragment less than the model mesh size and are accounted for in the results processing.

The modelling artifacts could be managed with a reduction in the model mesh size; however, recall that the goal of this modelling is to produce an efficient and practical solution for engineering purposes and increases in the number of mesh elements in a model dramatically increase model run times, making these sorts of models impractical for engineering projects in a consulting context.

### **3.2 Base Case Model Results**

After model stability had been tested and optimized, the base case model was executed, and the results were processed. Figure 19 presents the results of the fragmentation analysis on a percent passing chart for the first output time step for which the block has contacted the hopper (initial) and for the output time step for which motion has stopped (final). The percent passing chart shows block size (as a two-dimensional area) on the x-axis and percent passing on the y-axis, for a given block size, the curve describes the percent of blocks (by area) that are less than that block size. Typical data on percent passing charts for block size distributions for fragmentation show an s-shaped curve. It can be observed that the largest block size seen during the initial contact does not reduce in size considerably as the model progresses towards equilibrium resulting in a rotation of the curve around the largest fragment from initial to final rather than a translation.

Similar fragmentation changes are noted in literature during secondary fragmentation assessments of block cave mines (Pierce, 2010).

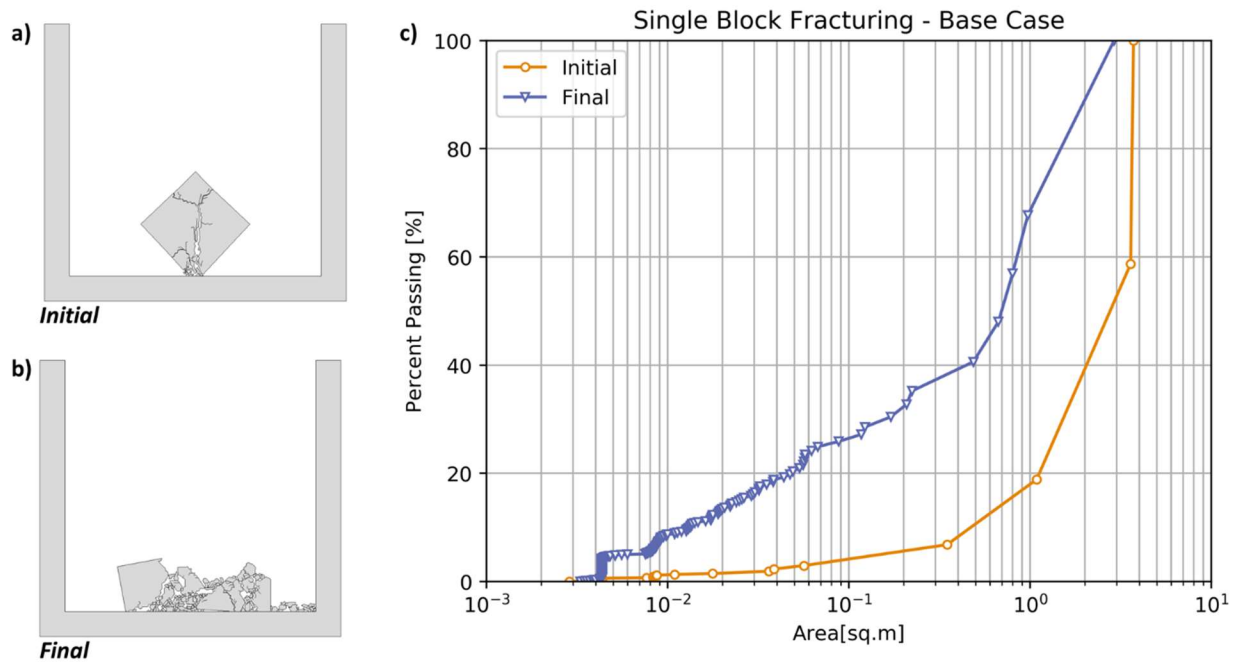


**Figure 19: Results of the Base Case FEM/DEM Model. a) Initial Rock Block Breakage at First Hopper Contact, b) Final Rock Block Breakage at Model Equilibrium and c) Percent Passing Chart Showing Initial and Final Fragmentation.**

### 3.3 Damping Sensitivity

Damping is a key factor in many different types of fracturing models including FEM/DEM models. Often, damping is difficult to approximate as there is no real-world equivalent, especially with the absence of real-world data. Therefore, a sensitivity analysis was conducted on the base case model to see the effects of different values of contact damping, top frequency damping, and rigid body motion damping.

The contact damping parameter is a value that reduces oscillations of edges between contact and non-contact states. In other words, edges that are close to each other, and very near to the search zone boundary will be damped such that the contact algorithm does not oscillate between assigning the elements as in contact or not in contact. Typical values for this parameter are suggested to be between 0 and 1 (Rockfield, 2011). Values of 0.1, 0.5, and 0.7 in addition to the base case value of 0.3 were tested during this assessment. The results of the analysis are shown in Figure 20.

Higher values of contact damping appear to reduce the number of deleted particles in the model due to the kinetic and elastic energy artifacts. It is unclear how many elements will break below the mesh size, so this would be a key parameter to adjust during model calibration. However, overall, the shape of the percent passing curves for each contact damping parameter appears to be similar, and therefore, it appears that this parameter only has a slight effect on the resulting fragmentation of the rock block.

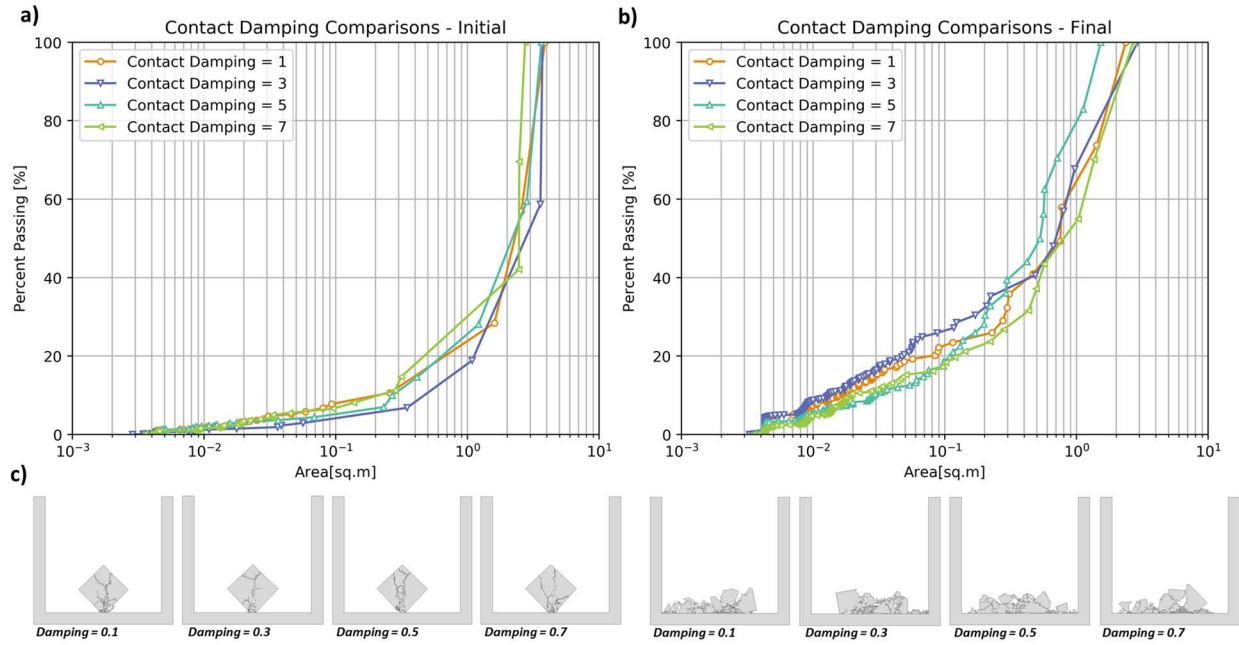


**Figure 20: Results of the Contact Damping Sensitivity Models. a) Initial Hopper Contact, b) Final Model Equilibrium. c) ELFEN Rock Block Visualisations.**

The top frequency damping parameter, which represents the proportion of high frequencies that will be critically damped, was tested using values of 1, 5, and 7 in addition to the base value of 2. Typical values for top frequency damping are suggested to be between 0 and 10 (Rockfield, 2011). The results of the analysis are shown in Figure 21.

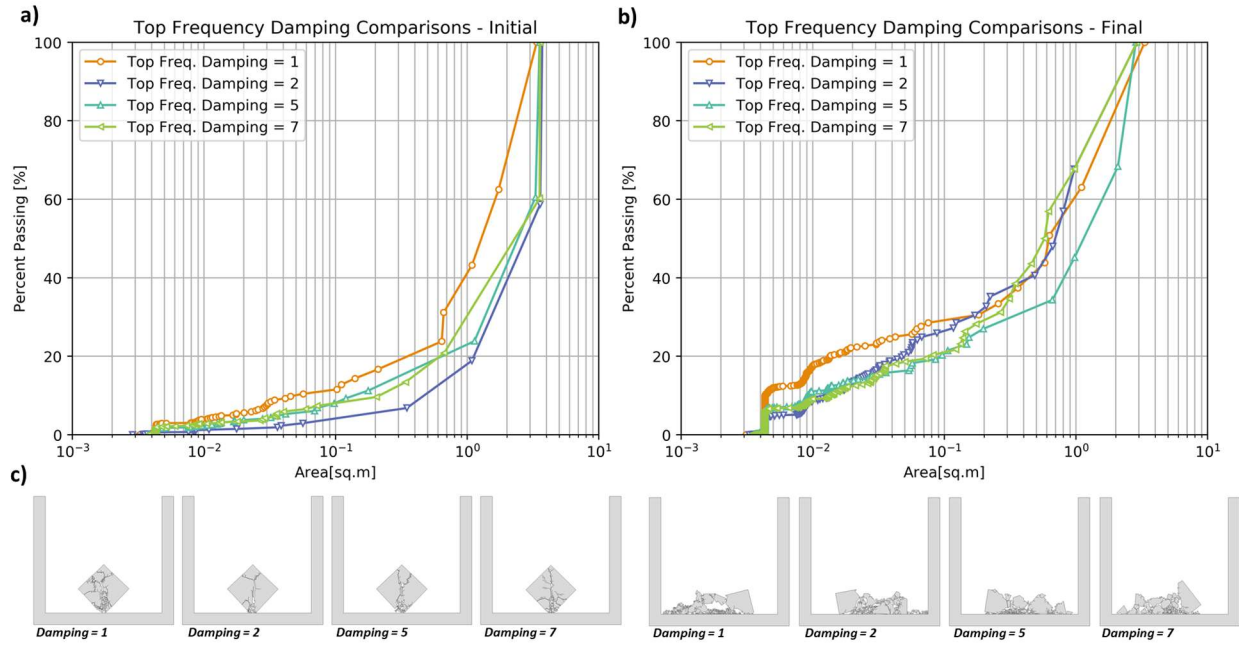


**Figure 21: Results of the Top Frequency Damping Sensitivity Models. a) Initial Hopper Contact, b) Final Model Equilibrium. c) ELFEN Rock Block Visualisations.**

Broadly, the top frequency damping parameter had minimal effect on the resulting block size distributions of the models. Similar shapes of the percent passing curves are noted for all the values of top frequency damping that were tested with slight variations in location that do not show a strong relationship to the value of the damping parameter. Similar to the contact damping, higher values of the damping parameter reduce the number of particles deleted due to modelling artifacts. Based on these results, the highest damping frequency (7) was used for the remainder of the analysis to improve model stability.

The rigid body motion damping, which is momentum dependent damping, was also tested using values of 1 and 3 in addition to the base value of 2. The suggested values for this damping parameter range between 0 and 3 (Rockfield, 2011).

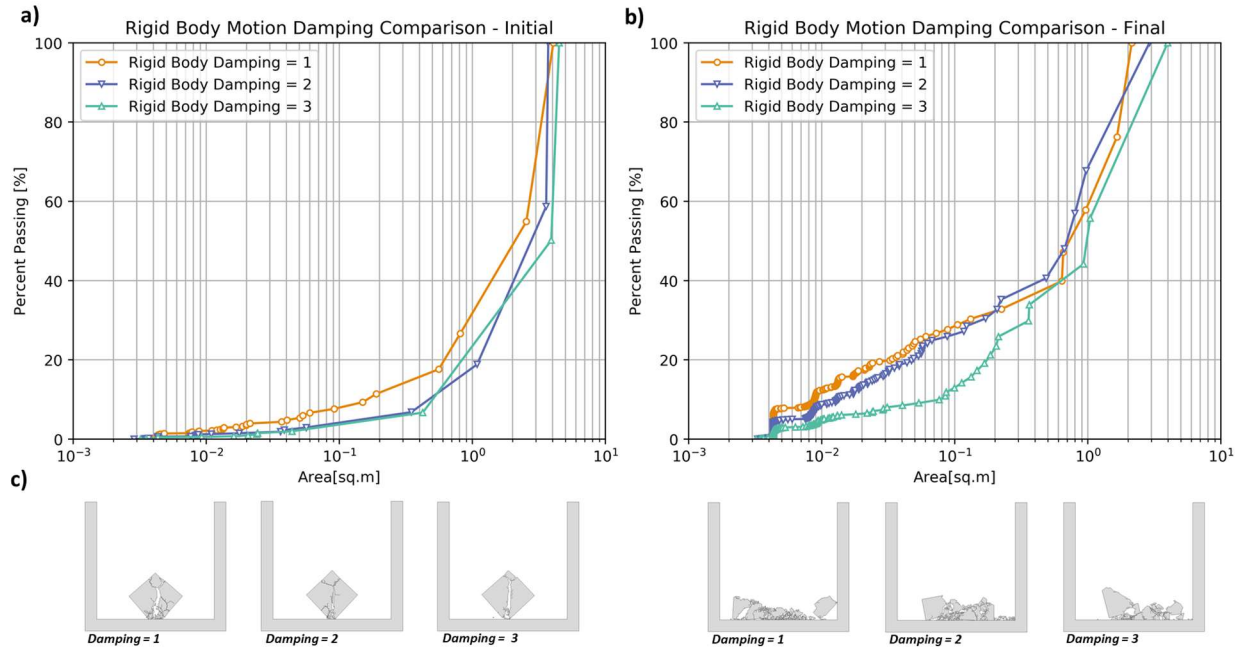


**Figure 22: Results of the Rigid Body Motion Damping Sensitivity Models. a) Initial Hopper Contact, b) Final Model Equilibrium. c) ELFEN Rock Block Visualisations.**

The rigid body motion damping has little effect on the models when reduced to 1, however, when increased to 3, the models slow in velocity considerably and the fragmentation decreases significantly. High values of rigid body damping were considered not representative of reality even though it would increase model stability and the base case of 2 was used for rigid body damping for the remainder of the assessment. This parameter shows the largest variation of the three damping parameters tested and particular attention should be paid to rigid body motion damping during any model calibration.

### 3.4 Chapter Summary

A gravity free-fall model was developed as a base case model to observe the fracturing of a brittle rock block with material parameters similar to those of an altered granitic rock typical of a

copper-porphyry deposit. The goal of these models was to produce a model that was quick to run with high levels of model stability for use in an engineering consulting context. The rock block is permitted to fall onto a fixed hopper and fracture. Fracturing is observed and the percent passing is plotted for the initial contact of the block with the hopper and at final model equilibrium. The models were not permitted to fracture below the initial mesh size in order to reduce model run times and increase stability. This inability to fracture below a specific size created velocity and deformation artifacts that were not representative of reality. These artifacts were removed through a deletion sequence and elements deleted were assumed to fracture below the initial mesh size. The results of the base case model show that the largest fragment developed after initial contact remains similar in size through the entire fracturing process resulting in a rotation of the block size curve around the largest fragment rather than a translation. Meaning, after initial contact, most of the breakage is smaller scale.

Damping tests were conducted on the model to observe the differences in fragmentation due to changes in damping parameters. Overall, the fragmentation curves have similar trends regardless of the value chosen, however, rigid body damping appeared to have a large effect on the resulting fragmentation. Rigid body damping should be the main parameter used to calibrate to real world data in the future.

## Chapter 4: Geometric Study

The geometric parameters of the model may affect the final fragmentation of the rock block and, therefore, a geometric study was conducted that includes variations in the block rotation and the shape of the hopper surface. The following sections outline the results of these models.

### 4.1 Block Rotation

When the rock block contacts the hopper, the initial orientation of the block may contribute to the fragmentation. The role of the rotation of the square rock block on initial and final fragmentation was explored by running several models with different rock block orientations. The zero-rotation condition was set to be when the flat edge of the block is parallel to the lower hopper surface. Models were created with 15-degree incremental rotations both clockwise (positive) and counter clockwise (negative). Therefore, a total of six models were used to determine the effect of rock block rotation at angles of -30-degrees, -15-degrees, 0-degrees, 15-degrees, 30-degrees, and 45-degrees (the base case).

The initial and final fragmentation curves resulting from these models are shown in Figure 23. Broadly, the initial fragmentation curves of the rock blocks for all models except the 0-degree model are similar. The 0-degree model shows high levels of initial fragmentation due to the line-contact of the rock block to the hopper. This high area contact allows for efficient energy transfer and the seeding of many fractures along the flat edge of the rock block, with aids in the fragmentation process and increases the degree of block breakage. The final fragmentation curves also show the 0-degree model has the highest fragmentation, with both the positive and negative 15-degree models showing slightly lower fragmentation, similar to the base case, and

the positive and negative 30-degree models showing the least fragmentation. The slight eccentricity of these 30-degree models breaks the block unevenly such that the largest fragment is more than half the size of the original block, the other models tend to break the block such that the largest fragment is half the size of the original block or less.

In order to better understand the differences between these models, the block size percentiles of D80, D50, and D20 were plotted against the rotation angle. These plots show the same trends noted from the fragmentation curves, but also show the similarities and differences in the model fragmentation with block rotation angle.

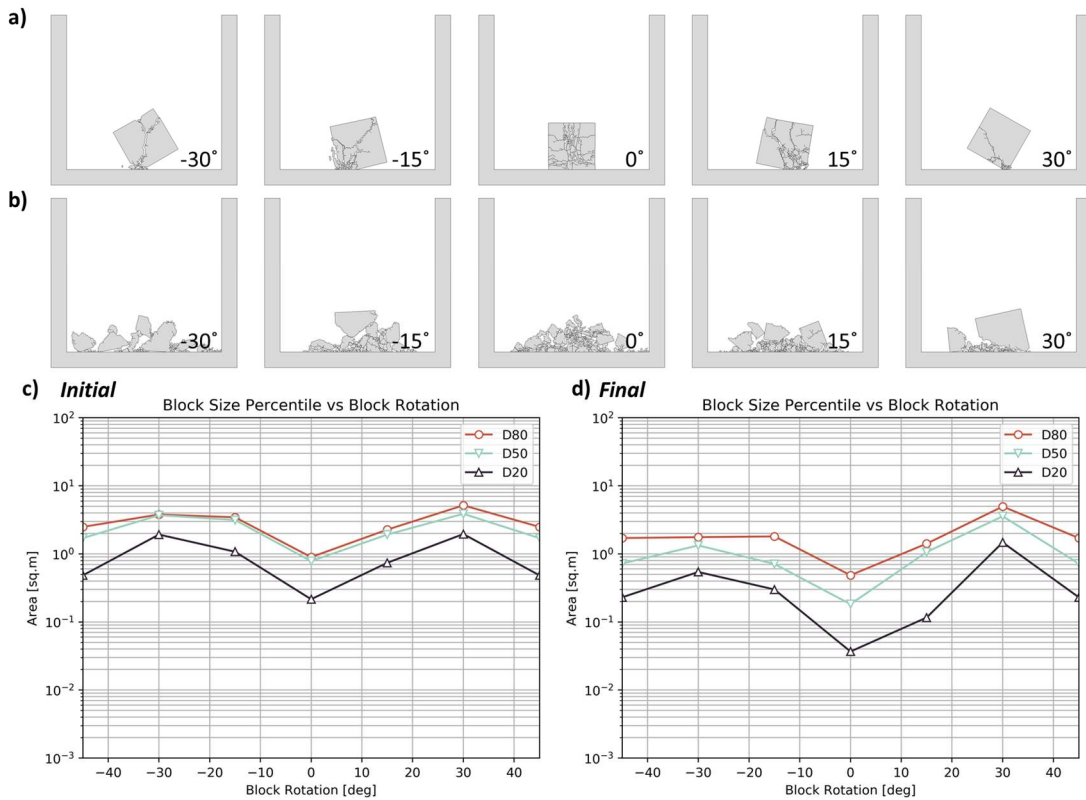


**Figure 23: Results of the Block Rotation Models a) Initial Hopper Contact ELFEN Visualisations, b) Final Model Equilibrium ELFEN Visualisations, c) Initial Block Size Percentiles by Rotation Angle, and d) Final Block Size Percentiles by Rotation Angle.**

Intuitively, it would be expected that the models would be perfectly symmetrical (i.e., the counter clockwise models would be the same as the clockwise models). Although they show similarities, the models are not identical indicating that the fracturing in these models is a random process and is slightly mesh dependent. The randomness and mesh dependency of these types of models is discussed in Munjiza (Munjiza, 2004), however; further study should be conducted to characterize these issues.

#### **4.2 Surface Curvature**

The curvature of the contact surface has also been explored in this study. Two additional models were made with the lower surface of the hopper being either concave or convex. The height of the apex of the concavity/convexity was modelled to be one metre.

The results of these models show that both the convex and concave models predict less fragmentation than the flat model. However, the mechanisms behind these reduced fragmentations appear to be different. In the concave model, the concavity reduces the ability of the rock blocks to travel laterally which results in less high velocity block-to-block interactions. In the convex model, after initial breakage, the rock blocks are immediately carried away from each other to the edges of the hopper limiting the block-to-block interaction. Overall, the concavity/convexity of the models reduces block-to-block interactions and therefore reduces the overall fragmentation.

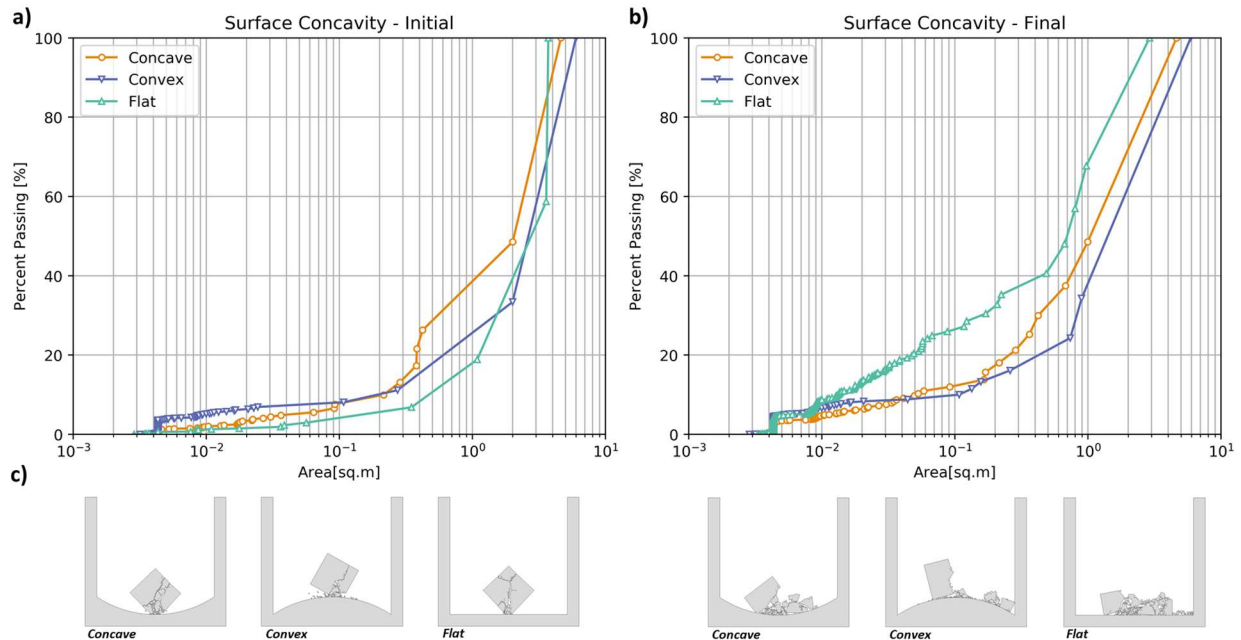


**Figure 24: Results of the Surface Concavity Testing. a) Initial Hopper Contact, b) Final Model Equilibrium.**

**c) ELFEN Rock Block Visualisations.**

### 4.3 Surface Roughness

An analysis of the roughness of the contact surface was conducted. To quantify the roughness of the surface, the Joint Roughness Coefficient (JRC) chart from Barton and Choubey (Barton & Choubey, 1977) was digitized. The JRC chart was developed to quantitatively describe the morphology of irregular joints. Ten (10) standard profiles were proposed based on the results of direct shear testing data and are shown in Figure 25.

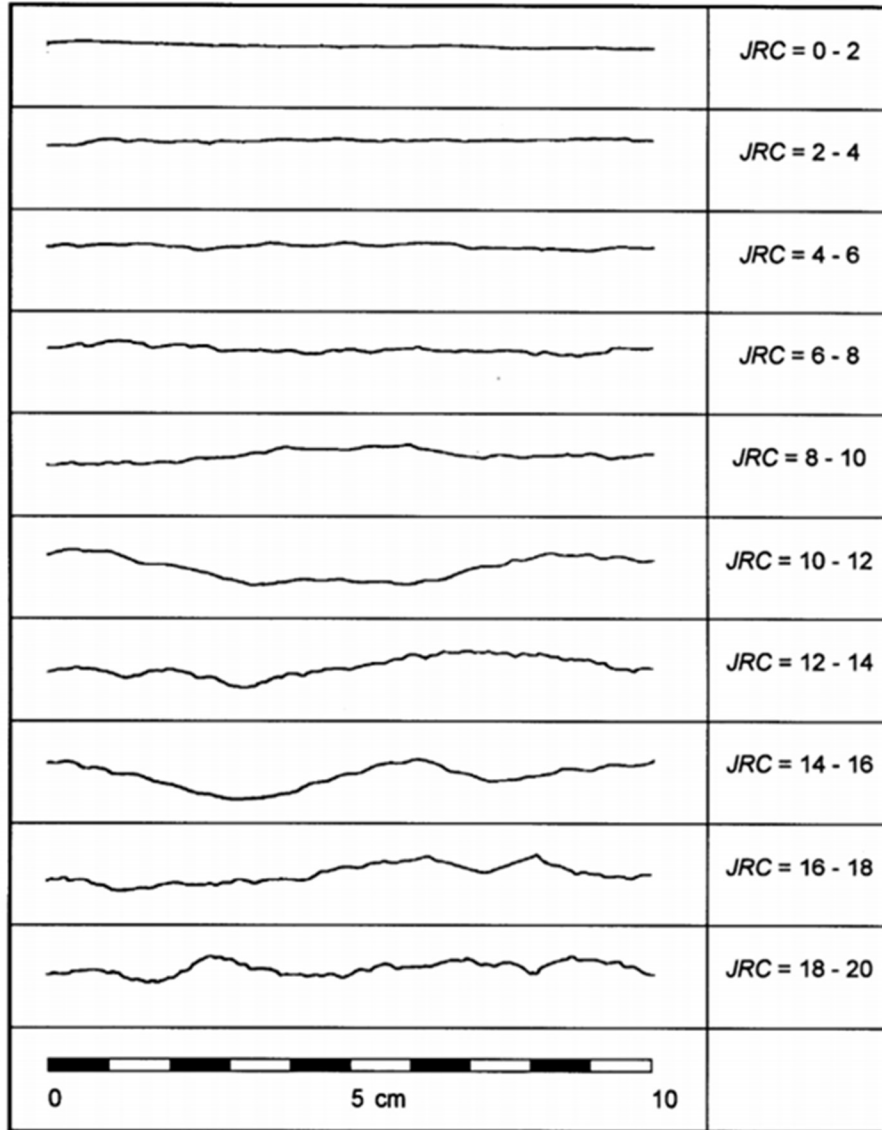


**Figure 25: Joint Roughness Coefficient Profiles (Barton and Choubey 1977)**

The JRC profiles represent surfaces that are 10 cm long, therefore, the profile needs to be scaled in order to fit the 10 m wide base of the hopper. The JCR value is not scale independent and from the chart in Figure 26 (Barton, N., Bandis, 1982), the profile needs to be scaled by a factor of 80 in the vertical direction and a factor of 100 in the horizontal direction in order to retain the

original JRC value when scaled from 10 cm to 10 m. These profiles were used as the hopper base geometry for 10 models ranging from JRC 0 through 18 in steps of 2.

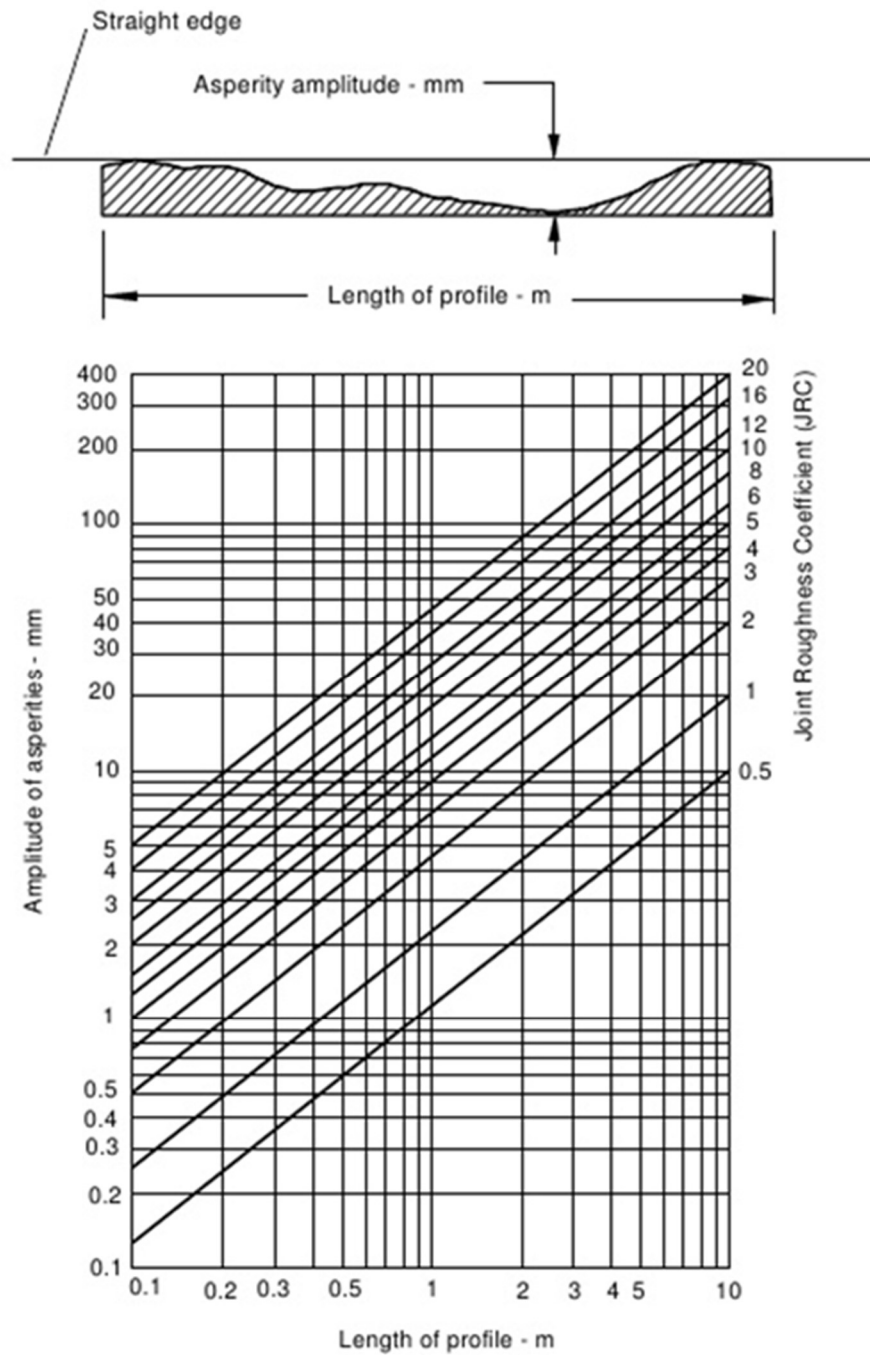
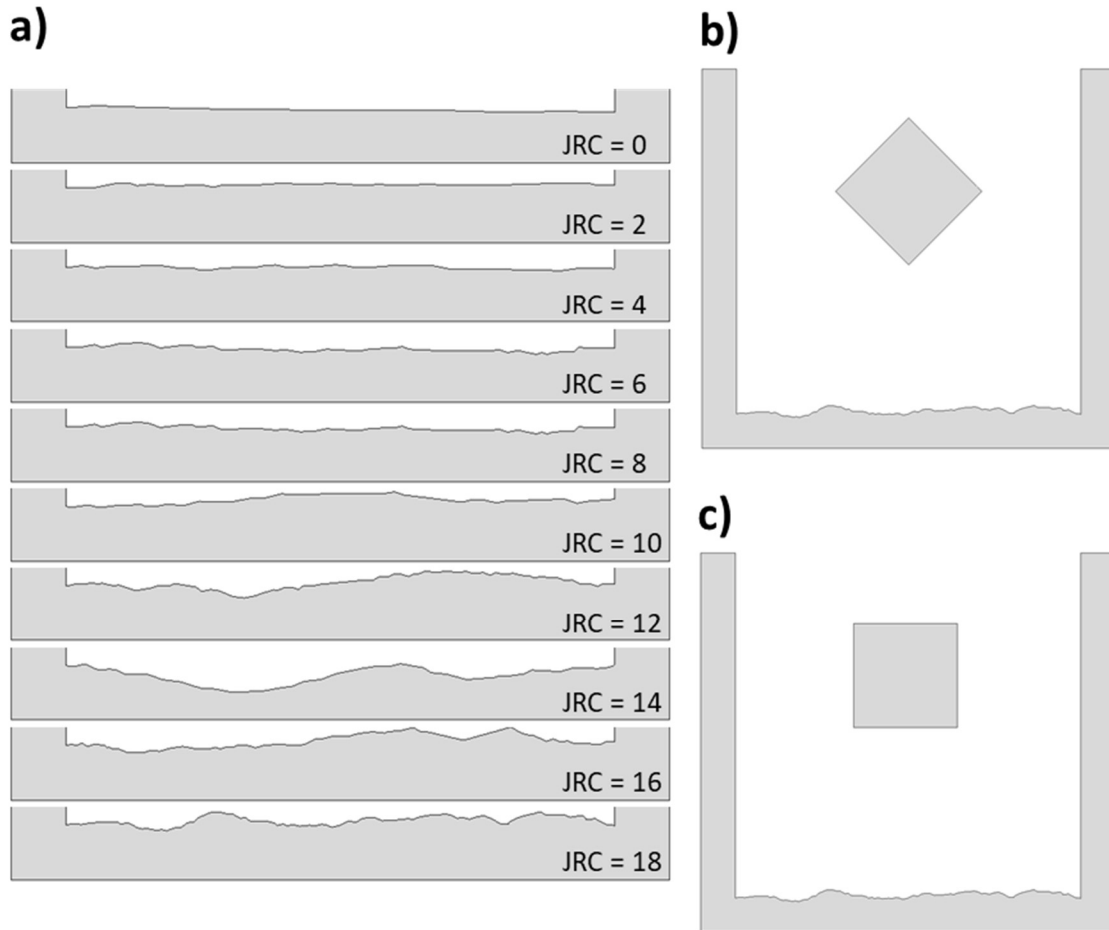


Figure 26: Joint Roughness Coefficient Scaling Chart (Barton, N., Bandis, 1982)

Block rotation angles of 0-degrees and 45-degrees were both modelled during the surface roughness testing to characterize the difference in line-contact versus point-contact of the blocks on the irregular surface. The model geometries are shown in Figure 27.



**Figure 27: Surface Roughness Model Geometry a) JRC Hopper Surfaces b) 45-degree Block Orientation over JRC = 18 Surface and c) 0-degree Block Orientation over JRC = 18 Surface**

The block size percentiles plotted against JRC for the initial and final states of both the 45-degree and 0-degree rotation models are shown in Figure 28. For the 45-degree block rotation model, the initial fragmentations are all similar, however, the final fragmentations show large

degrees of variabilities between the JRC values with a minimum block size observed at a JRC value of 8, and a maximum block size observed at a JRC value of 14.

The initial fragmentation of the 0-degree block rotation models is much more variable compared to the 45-degree block rotation models, with a minimum block size observed at a JRC value of 6 and a maximum block size observed at a JRC value of 16.

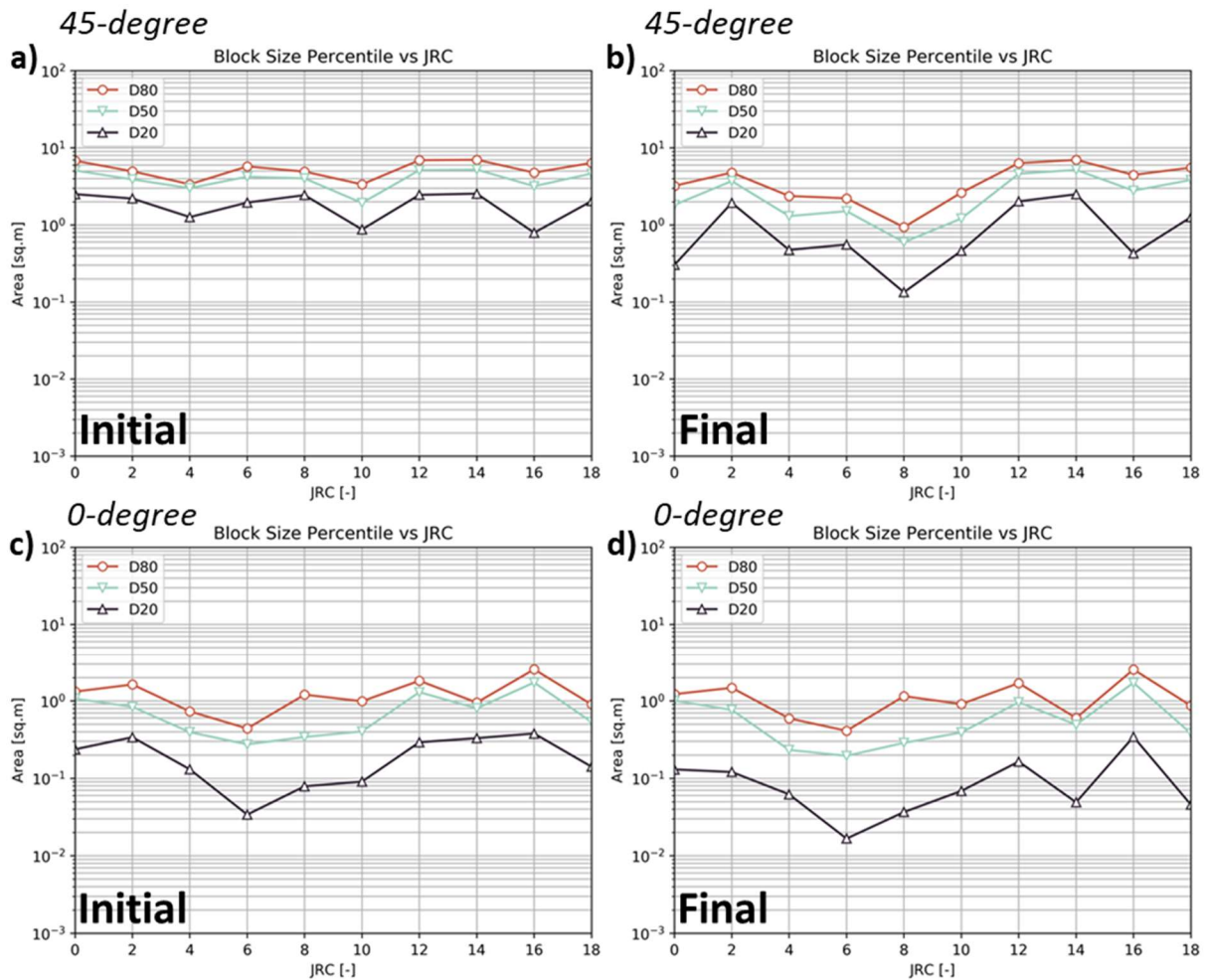


**Figure 28: Results of Surface Roughness Models a) Initial Block Contact for 45-degree Rotation Models b) Final Model Equilibrium for 45-degree Rotation Models c) Initial Block Contact for 0-degree Rotation Models, and d) Final Model Equilibrium for 0-degree Rotation Models.**

Overall, it appears the JRC number does not have any particular control on the resulting fragmentation, in other words, the JRC number itself does not accurately characterise how the differences in the roughness of the profiles translate to the fragmentation of the rock block. It should be noted that a large change in the surface characteristics of the JRC profiles can be seen starting around JRC of 10. For JRC profiles lower than 10, the surfaces show small scale roughness, for JRC 10 and higher, that roughness becomes more wavy and undulating in nature. The smaller scale roughness allows for fractures to initiate on the rock block at the contact point but reduces the overall movement of the blocks due to smaller blocks getting hung up in troughs in the roughness profile. The larger scale waviness and undulation works in a similar way to the initial block rotation and surface curvature, by changing the angle of contact the block has with the hopper surface and the directions in which the blocks travel. These two levels of roughness are not distinct in the JRC assignment and therefore contribute to the lack of correlation between JRC and block fragmentation. Another method of characterising the roughness of the hopper surface may show stronger fragmentation trends.

#### **4.4 Chapter Summary**

The geometry of the modelled was altered to test the fragmentation results due to rock block rotation, the curvature of the hopper surface, and the roughness of the hopper surface. Rock block rotations that result in slight eccentricities of the block contact result in less fragmentation than geometries that allow for symmetrical contact. The flat line-to-line contact of the rock block with the hopper produces the highest degree of fracturing. Convexities and concavities in the hopper surface both reduce the fragmentation of the rock block by reducing block-to-block

interactions. However, convexity reduces these interactions by carrying blocks away from each other after initial contact and concavity reduce interactions by holding blocks together and reducing block velocities. Lastly, the JRC number does not describe the change in fragmentation due to the roughness of the hopper surface well and a meaningful correlation was not found. Clear changes in fragmentation were observed due to small-scale roughness and large-scale waviness, but another way of describing this roughness may provide for a better prediction of fragmentation.

## Chapter 5: Fractal Block Breakage Relationships

It is clear from the results shown in the previous section, rock block breakage due to gravity free-fall results in fragmentation of a rock block that cannot be described as perfect splitting (i.e., two or more equal sized rock blocks being produced). The common methods for estimating secondary fragmentation assume perfect block splitting. Therefore, there is a need to understand the breakage of rock blocks and their final size distributions in order to accurately describe the splitting of a rock block for use in block cave fragmentation assessments. A concept that has appeared in a recent study of rockfall is the fractal model of block size (Gili et al., 2016; Matas et al., 2020; Ruiz-Carulla & Corominas, 2020). This theory presents a size invariable final block size distribution, and the resultant fragments will have a relationship to the initial size of the block that follows a power trend.

In order to test this theory and its applicability to the FEM/DEM models presented in the previous section, a series of models were developed utilizing different size rock blocks. The original model has a block side length of 3 m. Three additional models were created with block side lengths of 1 m, 1.5 m, and 6 m, or size factors of 0.33, 0.5, and 2. The four models, including the base case model, are shown in Figure 29.

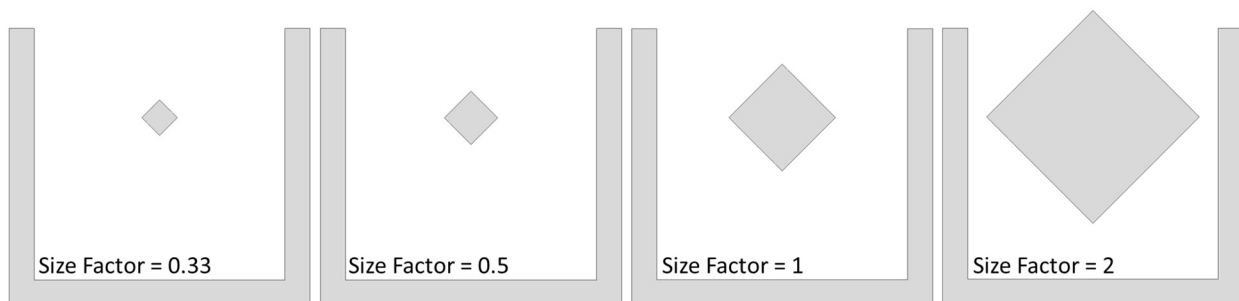


**Figure 29: Variable Size Models**

Each of these models was run and the resulting fragmentation was calculated. Ruiz-Carulla and Corominas (Ruiz-Carulla & Corominas, 2020) propose a fractal block size model due to rock fall as shown in Equation 16, where  $V_n$  is the volume of the  $n^{\text{th}}$  fragment,  $V_0$  is the initial block size,  $L_{\text{max}}$  is the largest fragment generated as a percentage of the original volume,  $n$  is number of fragments from 1 to infinite, and  $D_f$  is the fractal dimension.

$$V_n = V_0 L_{\text{max}} n^{-1/D_f} \quad \text{Equation 16}$$

Rearranging this equation such that the number of fragments ( $n$ ) is the independent variable, we can describe the number of blocks as a function of the ratio of the final and initial block size (Equation 17).

$$n = \left[ \frac{1}{L_{\text{max}}} \right]^{-D_f} \left( \frac{V_n}{V_0} \right)^{-D_f} \quad \text{Equation 17}$$

The final equilibrium results of the four size models are plotted on a log-log plot in Figure 30 with number of fragments on the y-axis and normalized fragment area on the x-axis. A power law trend was fit to these data giving a fractal dimension ( $D_f$ ) of 0.69 and a coefficient of 0.55, which results in a  $L_{\text{max}}$  of 0.42. In other words, the maximum expected fragment size for rock blocks with these properties would be 42% of the initial block size. Following the fractal trend downward, it is predicted that two fragments 15.4% of the original block size can be expected, and three fragments 8.6% of the original block size can be expected and so forth. As shown in the figure, the models of size ratios 0.5, 1, and 2 fit very closely to the power law trend, with the 0.33 size ratio following the general slope of the trend but in a different location (i.e., a different  $L_{\text{max}}$  value may be more appropriate for this model). This is most likely due to the reduction in the size of the model reducing the stress exhibited on the block resulting in less fracturing.

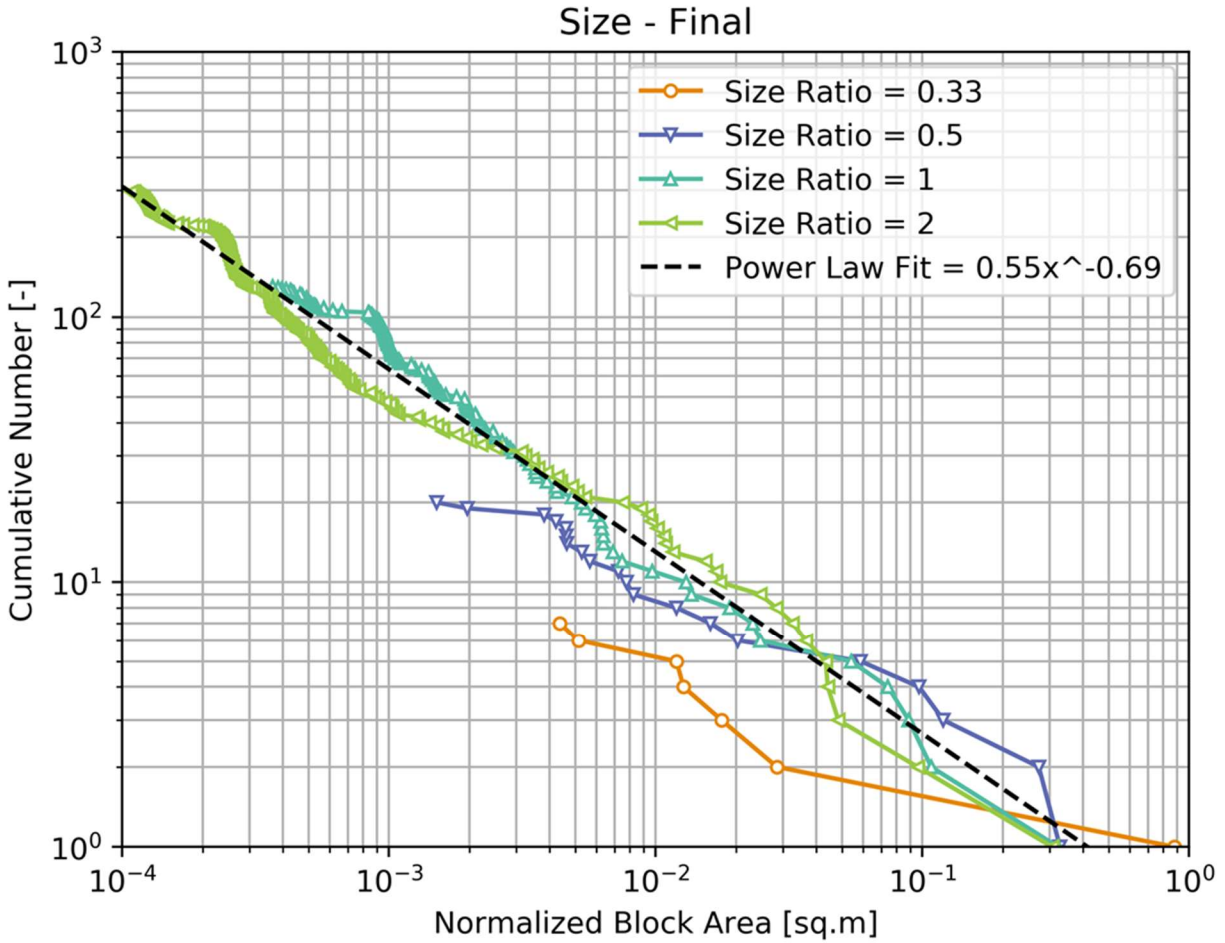


**Figure 30: Log-Log Plot of Final Size Distribution of Variable Size Models with Power Law Fit**

To observe differences in the fractal relationships, the block rotation, surface concavity, and surface roughness models were all plotted on the log-log chart in Figure 31 through Figure 33. The models all appear to show similarities in the fractal dimension, so for sake of comparison, the fractal dimension was fixed as 0.69 and the power trends were fit to each model by varying the coefficient. The models appear to conform well to the fractal dimensions for lower normalized block areas and deviate away from the trend at higher block areas. In other words, the fractal trend predicts the production of small fragments well. An explanation for this phenomenon could be attributed to the method of block breakage used in these models. Since

these models simulate the impact of rock blocks, the initial block breakage may be the controlling factor on the larger blocks which does not follow a natural fractal relationship, while smaller blocks are formed by block attrition and breakdown which may follow more natural fractal block forming relationships. In the case of secondary fragmentation, the majority of block breakage can be attributed to block attrition and breakdown rather than discrete block splitting events, so a fractal relationship to predict block sizes may be appropriate.

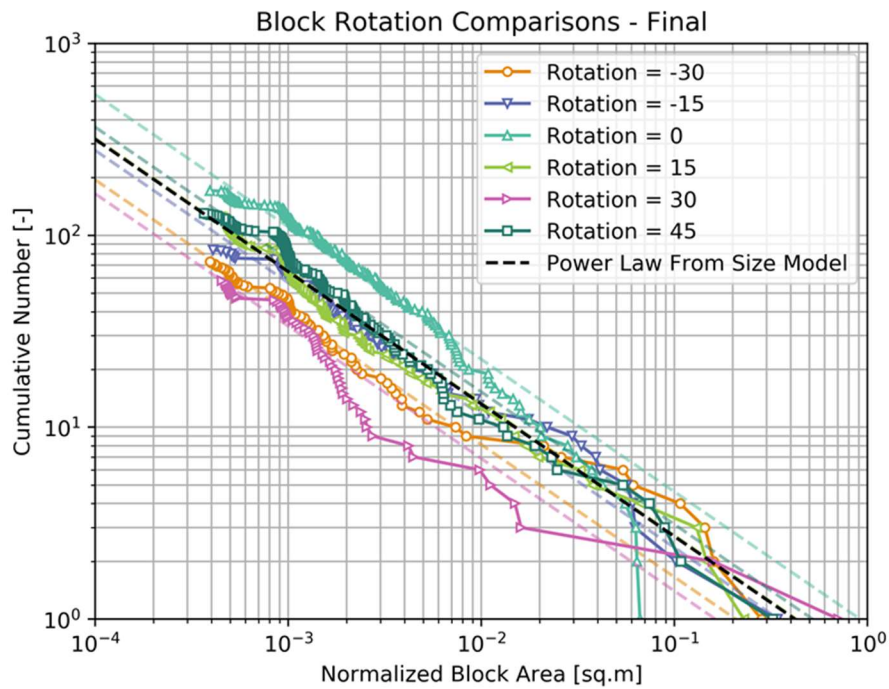


Figure 31: Log-Log Plot of Block Rotation Models

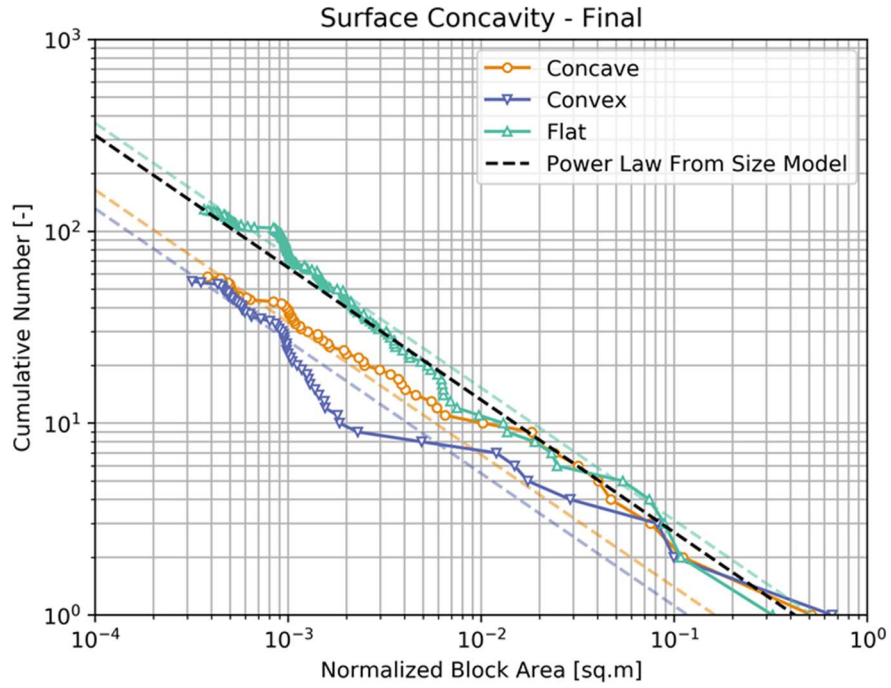


Figure 32: Log-Log Plot of Surface Curvature Models

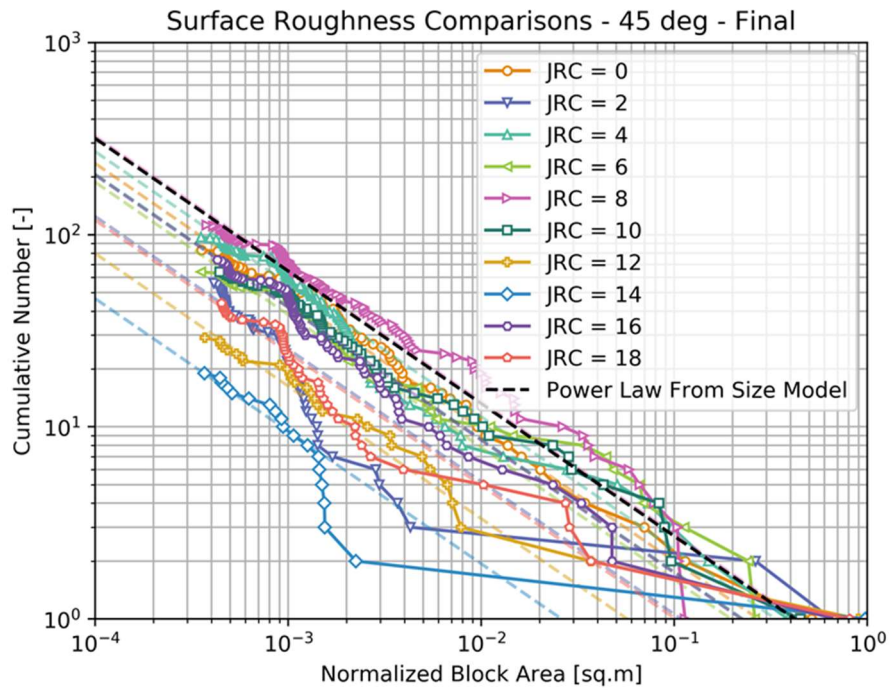


Figure 33: Log-Log Plot of Surface Roughness Models

## 5.1 Chapter Summary

There is a need to develop a relationship to predict block breakage and size variable models plotting on a similar fractal trend is a promising result for the development of a fractal relationship of rock block breakage. It appears that the models presented in this thesis follow power trends at the finer portion of the fragmentation curves and do not conform as well at the coarser end. The method of rock block breakage may be the reason for this observation. As most block breakage attributed to secondary fragmentation is due to block attrition rather than discrete high-energy block splitting events, secondary fragmentation distributions may follow a natural fractal trend and further research is justified in this area.

## Chapter 6: Conclusion

### 6.1 Research Summary

The understanding of how rock blocks break to form smaller fragments can be informed by rock mass strength criteria such as the Mohr-Columb criterion (Labuz & Zang, 2012), the Hoek-Brown criterion (Hoek et al., 2002), and the tri-linear failure envelope (Bewick et al., 2019).

Methods to stochastically estimate how a rock block will break have been utilized for estimating block cave fragmentation, particularly in the case of the popular fragmentation software, BCF (Esterhuizen, 2005). However, to date, there has been little numerical modelling to observe how a rock block breaks with a focus on resulting block volumes, and many of these block breakage estimates are based on empiricism.

The research described above aimed to develop hybrid FEM/DEM models for gravity free-fall of a rock block and the resulting block fragmentation through the lens of block volume estimates and predictions. Efficient and useful models were the goal and through model simplification and deletion sequences to reduce model instability, efficient block breakage models were developed that can be used effectively in a consulting context.

Sensitivity analysis of damping parameters showed that these models are not particularly sensitive to the three different types of damping employed. Although there is some variation at different levels of damping, with no physical modelling to compare these values to, calibration should be done on a project-to-project basis.

The geometric study varied the orientation of the rock block, and the shape of the hopper surface to observe changes in block breakage behaviour. Overall, the rotation angle of the rock block and

how the block contacts the hopper surface have a large effect on the initial and final fragmentation of the block. Surface concavity also affects the resulting fragmentation distributions. In the concave case, blocks travel less and have less opportunity to interact. In the convex case, blocks move away from each other after initial contact and have less opportunity to interact. Varying the surface roughness of the hopper was done using JRC as an analogue. No strong relationship was observed between JRC and the final block breakage indicating that the JRC number does not capture the variability in surface roughness well enough for the purposes of this study.

The fractal relationships of block sizes were also explored by modelling three additional block sizes. Overall, when plotted on a log-log plot, the four block sizes all follow a similar fractal trend, indicating that the breakage of a rock block may be size invariable. When plotting other models (e.g., block rotation models, JRC models, and concavity models), similar fractal slopes are seen on the finer end of the fragmentation distributions, but the relationships differ on the coarse end.

## **6.2 Main Findings and Conclusions**

The main findings of this research are summarized as follows:

- First and foremost, block breakage and fragmentation are not trivial and are affected by a variety of different parameters. For example, slight changes in the contact angle between a block corner and a surface have large effects on the resulting fragmentation distributions. Therefore, when block breakage estimates are being made, ranges of possible outcomes should be considered, rather than overly predictive outcomes.

- Current secondary fragmentation estimation strategies focus primarily on determining if a block will break and when a block has been determined to split, simplistic block breakage assumptions are used (e.g., the block splits in half, in the case of BCF). This work shows that simple block breakage is not the case and refining how we model block breakage will serve to provide better estimates of secondary fragmentation for block caving.
- FEM/DEM models can be simplified and utilized for more time-sensitive engineering work and are not exclusive to academia. Assumptions need to be introduced for this to be the case, and validation with real world data should be completed to verify if these assumptions are reasonable.
- Block breakage appears to show fractal relationships similar to those seen by academics studying rock fall (Gili et al., 2016; Matas et al., 2020; Ruiz-Carulla & Corominas, 2020). When the models only vary in size, a strong fractal relationship is observed. When other parameters are varied, the finer fraction of fragmentation distributions fit well to these relationships but the coarser fraction deviates. A preliminary hypothesis for this outcome is possibly due to the coarser fraction being a product of the mechanism for which the block breaks (i.e., gravity free-fall, in this case) and the finer fraction is more reliant on block attrition and may follow more natural fractal laws. Future work should focus on these relationships.

### **6.3 Limitations and Assumptions**

The research described previously is subject to the following limitations and assumptions:

- The obvious limitation of this analysis is that this study is purely numerical modelling based and not yet compared to real world data. Although FEM/DEM and ELFEN

modelling has been extensively used, verified, and validated by other academics (Cai & Kaiser, 2004; Elmo et al., 2013; Hamdi et al., 2015; Karami & Stead, 2008; Vyazmensky, Elmo, et al., 2010) and the fractal relationships developed from rock fall studies (Gili et al., 2016; Matas et al., 2020; Ruiz-Carulla & Corominas, 2020) appear to fit well with the modelling data, this research uses different assumptions and includes the deletion sequence for increased model stability which has yet to be verified.

- The block breakage relationships developed in this study assume that the gravity free-fall of a single rock block is comparable to the conditions that may occur during secondary fragmentation in block caving. In reality, there are a variety of different processes that can break a block in secondary fragmentation, including block compression and rilling. This research is only a starting point in understanding how blocks break in secondary fragmentation.
- Each of these models was only run once, due to the difficulty in randomizing the mesh in ELFEN. Running a statistically significant number of models with variable meshing would allow for a better understanding of the variability of the resulting fragmentation distributions and their mesh dependency.

#### **6.4 Recommendations for Future Work**

Future work stemming from this research could include:

- Physical tests to verify the results of the FEM/DEM modelling, which would allow for more confidence in utilizing these techniques and output relationships.
- As FEM/DEM technology improves, the ability to run many models with variable meshing would allow for a more statistically significant number of iterations of each

block breakage model to be run, which would provide further confidence in the resulting range of fragmentation distributions that can be expected.

- Utilizing the fractal relationships of block breakage in the current methodologies for secondary fragmentation estimates (e.g., BCF and the DFN method), may provide for better predictions of secondary fragmentation that fit better to data collected from active mines.
- Further studies of different block breakage mechanisms and how the resulting fragmentation fits the fractal relationships would be useful. For example, analysis of the fractal relationships of the resulting fragmentation from the FEM/DEM compression of rock blocks shown in Figure 14 (Rogers et al., 2010) would be of interest.

## Bibliography

- Barton, N., Bandis, S. C. (1982). Effects of block size on the shear behaviour of jointed rock. *23rd U.S. Symp. on Rock Mechanics*, 739–760.
- Barton, N., & Choubey, V. (1977). The shear strength of rock joints in theory and practice. *Rock Mechanics Felsmechanik Mécanique Des Roches*, 10(1–2), 1–54.  
<https://doi.org/10.1007/BF01261801>
- Bewick, R. P., Kaiser, P. K., & Amann, F. (2019). Strength of massive to moderately jointed hard rock masses. *Journal of Rock Mechanics and Geotechnical Engineering*, 11(3), 562–575. <https://doi.org/10.1016/j.jrmge.2018.10.003>
- Brobst, T., Utah, K., Mine, B. C., & States, U. (2008). Update on the Bingham Canyon mine underground studies. *MassMin2008, June*.
- Brown, E. T. (2003). *Block caving geomechanics*. Julius Kruttschnitt Mineral Research Centre.
- Brunton, I., Lett, J. L., & Thornhill, T. (2016). Fragmentation Prediction and Assessment at the Ridgeway Deeps and Cadia East Cave Operations. *MassMin2016*.
- Cai, M., & Kaiser, P. K. (2004). Numerical simulation of the Brazilian test and the tensile strength of anisotropic rocks and rocks with pre-existing cracks. *International Journal of Rock Mechanics and Mining Sciences*, 41(SUPPL. 1), 1–6.  
<https://doi.org/10.1016/j.ijrmms.2004.03.086>
- Cai, M., Kaiser, P. K., Uno, H., Tasaka, Y., & Minami, M. (2004). Estimation of rock mass deformation modulus and strength of jointed hard rock masses using the GSI system. *International Journal of Rock Mechanics and Mining Sciences*, 41(1), 3–19.  
[https://doi.org/10.1016/S1365-1609\(03\)00025-X](https://doi.org/10.1016/S1365-1609(03)00025-X)
- Carranza-Torres, C. (1998). *Study of the relationship between caved column height and pressure*

at the cave base. Itasca Consulting Group.

Chiles, J. P., Wackernagel, H., Beucher, H., Lantuejoul, C., & Elion, P. . (2008). Estimating Fracture Density from a Linear or Areal Survey. *Proceedings of the Eighth International Geostatistics Congress, 1*, 535–544.

Chitombo, G. P. (2010). Cave mining: 16 years after Laubscher's 1994 paper "Cave mining - State of the art." *Transactions of the Institutions of Mining and Metallurgy, Section A: Mining Technology*, 119(3), 132–141.

<https://doi.org/10.1179/174328610X12820409992255>

Dershowitz, W., Lee, G., Geier, J., & LaPointe, R. P. (1998). *FracMan: Interactive Discrete Fracture Data Analysis, Geometric Modeling and Exploration Simulation. User Documnetation*. Golder Associates Ltd.

Diederichs, M. S. (1999). *Instability of Hard Rockmasses: The Role of Tensile Damage and Relaxation*. University of Waterloo.

Eberhardt, E., Stead, D., & Coggan, J. S. (2004). Numerical analysis of initiation and progressive failure in natural rock slopes-the 1991 Randa rockslide. *International Journal of Rock Mechanics and Mining Sciences*, 41(1), 69–87. [https://doi.org/10.1016/S1365-1609\(03\)00076-5](https://doi.org/10.1016/S1365-1609(03)00076-5)

Eberhardt, E., Stead, D., Stimpson, B., & Read, R. S. (1998). Identifying crack initiation and propagation thresholds in brittle rock. *Canadian Geotechnical Journal*, 35(2), 222–233. <https://doi.org/10.1139/t97-091>

Elmo, D., Rogers, S., Beddoes, R., & Catalan, A. (2010). An integrated finite/discrete element method – discrete fracture network synthetic rock mass approach for the modelling of surface subsidence associated with panel cave mining at the Cadia East underground

- project. *Caving 2010*, 167–179. [https://doi.org/10.36487/acg\\_rep/1002\\_9\\_elmo](https://doi.org/10.36487/acg_rep/1002_9_elmo)
- Elmo, D., Rogers, S., Stead, D., & Eberhardt, E. (2014). Discrete fracture network approach to characterise rock mass fragmentation and implications for geomechanical upscaling. *Mining Technology*, 123(3), 149–161. <https://doi.org/10.1179/1743286314Y.0000000064>
- Elmo, D., Schlotfeldt, P., Beddoes, R., & Roberts, D. (2011). Numerical simulations of scale effects under varying loading conditions for naturally fractured rock masses and implications for rock for rock mass strength characterization and the design of overhanging rock slopes. *45th US Rock Mechanics / Geomechanics Symposium*.
- Elmo, D., & Stead, D. (2010). An integrated numerical modelling-discrete fracture network approach applied to the characterisation of rock mass strength of naturally fractured pillars. *Rock Mechanics and Rock Engineering*, 43(1), 3–19. <https://doi.org/10.1007/s00603-009-0027-3>
- Elmo, D., Stead, D., Eberhardt, E., & Vyazmensky, A. (2013). Applications of Finite/Discrete Element Modeling to Rock Engineering Problems. *International Journal of Geomechanics*, 13(5), 565–580. [https://doi.org/10.1061/\(asce\)gm.1943-5622.0000238](https://doi.org/10.1061/(asce)gm.1943-5622.0000238)
- Elmo, D., Stead, D., & Rogers, S. (2008). Quantitative analysis of fractured rock masses using a discrete fracture network approach : Characterisation of natural fragmentation and implications for current rock mass classification systems. *5th International Conference and Exhibition on Mass Mining, June*.
- Esterhuizen, G. S. (2005). *A Program to Predict Block Cave Fragmentation; Technical Reference and User's Guide* (3.05; Issue December).
- Gili, J. A., Ruiz, R., Matas, G., Corominas, J., Lantada, N., Núñez, M. A., Mavrouli, O., Buill, F., Moya, J., Prades, A., & Moreno, S. (2016). Experimental study on rockfall

- fragmentation: In situ test design and first results. *Landslides and Engineered Slopes. Experience, Theory and Practice*, 2, 983–990. <https://doi.org/10.1201/b21520-116>
- Griffith, A. . A. . (1920). The Phenomena of Rupture and Flow in Solids. *Philosophical Transactions of the Royal Society of London. Series A, Containing Papers of a Mathematical or Physical Character*, 221(1921), 163–198.
- Hamdi, P., Stead, D., & Elmo, D. (2015). Characterizing the influence of stress-induced microcracks on the laboratory strength and fracture development in brittle rocks using a finite-discrete element method-micro discrete fracture network FDEM- $\mu$ DFN approach. *Journal of Rock Mechanics and Geotechnical Engineering*, 7(6), 609–625. <https://doi.org/10.1016/j.jrmge.2015.07.005>
- Hoek, E. (1968). Brittle failure of rock. In K. G. Stagg & O. C. Zienciewics (Eds.), *Rock mechanics in engineering practice* (pp. 99–124). Wiley.
- Hoek, E., & Brown, E. T. (1980a). Underground Excavations in Rock. In *Institution of Mining and Metallurgy*. Institution of Mining and Metallurgy.
- Hoek, E., & Brown, E. T. (1980b). Empirical strength criterion for rock masses. *International Journal of Rock Mechanics and Mining Sciences & Geomechanics Abstracts*, 18(2), 23. [https://doi.org/10.1016/0148-9062\(81\)90766-X](https://doi.org/10.1016/0148-9062(81)90766-X)
- Hoek, E., & Brown, E. T. (2019). The Hoek–Brown failure criterion and GSI – 2018 edition. *Journal of Rock Mechanics and Geotechnical Engineering*, 11(3), 445–463. <https://doi.org/10.1016/j.jrmge.2018.08.001>
- Hoek, E., Carranza, C., & Corkum, B. (2002). Hoek-brown failure criterion – 2002 edition. *Proceedings of the NARMS-TAC Conference*, 267–273.
- Hoek, E., Kaiser, P. K., & Bawden, W. F. (2000). *Support of Underground Excavations in Hard*

*Rock* (Vol. 53, Issue 9). <https://doi.org/https://doi-org.ezproxy.library.ubc.ca/10.1201/b16978>

Jakubec, J. (2014). Fragmentation estimates using BCF software - Experiences and pitfalls.

*Caving*.

Karami, A., & Stead, D. (2008). Asperity degradation and damage in the direct shear test: A hybrid FEM/DEM approach. *Rock Mechanics and Rock Engineering*, 41(2), 229–266.

<https://doi.org/10.1007/s00603-007-0139-6>

Klerck, P. A. (2000). *The finite element modelling of discrete fracture in quasi-brittle materials*.

Ph.D. Thesis - Swansea University - Wales.

Klerck, P. A., Sellers, E. J., & Owen, D. R. J. (2004). Discrete fracture in quasi-brittle materials

under compressive and tensile stress states. *Computer Methods in Applied Mechanics and*

*Engineering*, 193(27–29), 3035–3056. <https://doi.org/10.1016/j.cma.2003.10.015>

Labuz, J. F., & Zang, A. (2012). Mohr-Coulomb failure criterion. *Rock Mechanics and Rock*

*Engineering*, 45(6), 975–979. <https://doi.org/10.1007/s00603-012-0281-7>

Lajtai, E. Z., & Lajtai, V. N. (1974). The evolution of brittle fracture in rocks. *International*

*Journal of Rock Mechanics and Mining Sciences & Geomechanics Abstracts*, 11(6), 115.

[https://doi.org/10.1016/0148-9062\(74\)90155-7](https://doi.org/10.1016/0148-9062(74)90155-7)

Laubscher, D. (2000). a Practical Manual on Block Caving. *A Practical Manual on Block*

*Caving*, 89–100.

Laubscher, D. H. (1994). Cave mining - the state of the art. *The Journal of the South African*

*Institute of Mining and Metallurgy*, 94(10), 279–294.

Matas, G., Lantada, N., Corominas, J., Gili, J., Ruiz-Carulla, R., & Prades, A. (2020). Simulation

of full-scale rockfall tests with a fragmentation model. *Geosciences (Switzerland)*, 10(5).

<https://doi.org/10.3390/geosciences10050168>

- Munjiza, A. (2004). The combined finite-discrete element method. In *The Combined Finite-Discrete Element Method*. John Wiley & Sons, Ltd. <https://doi.org/10.1002/0470020180>
- Ngidi, N., & Pretorius, D. (2010). Impact of poor fragmentation on cave management. *Caving*, 593–601. [https://doi.org/10.36487/acg\\_rep/1002\\_41\\_ngidi](https://doi.org/10.36487/acg_rep/1002_41_ngidi)
- Nicholas, D., & Srikant, A. (2004). *Assessment of primary fragmentation from drill core data*. August, 22–25.
- Pierce, M. (2010). *A model for gravity flow of fragmented rock in block caving mines* (Issue September 2010) [Ph.D. Thesis - The University of Queensland]. [http://espace.library.uq.edu.au/view/UQ:215665%5Cnhttp://www.isrm.net/fotos/gca/13388862502013\\_thesis\\_summary\\_mpierce.pdf](http://espace.library.uq.edu.au/view/UQ:215665%5Cnhttp://www.isrm.net/fotos/gca/13388862502013_thesis_summary_mpierce.pdf)
- Rockfield. (2011). *ELFEN 4.4 Explicit Manual* (4.4, Issue August). Rockfield Software Ltd. <https://www.rockfieldglobal.com/>
- Rogers, S., Elmo, D., Webb, G., & Catalan, A. (2010). A discrete fracture network based approach to defining in situ, primary and secondary fragmentation distributions for the Cadia East panel cave project. *Caving 2010*, 425–439. [https://doi.org/10.36487/acg\\_rep/1002\\_29\\_rogers](https://doi.org/10.36487/acg_rep/1002_29_rogers)
- Ruiz-Carulla, R., & Corominas, J. (2020). Analysis of Rockfalls by Means of a Fractal Fragmentation Model. *Rock Mechanics and Rock Engineering*, 53(3), 1433–1455. <https://doi.org/10.1007/s00603-019-01987-2>
- Srikant, A., Nicholas, D. E., & Rachmad, L. (2004). Visual estimation of fragment size distributions in the DOZ block cave. *Massmin 2004*, August, 22–25.
- Stead, D., Eberhardt, E., & Coggan, J. S. (2006). Developments in the characterization of

- complex rock slope deformation and failure using numerical modelling techniques. *Engineering Geology*, 83(1–3), 217–235. <https://doi.org/10.1016/j.enggeo.2005.06.033>
- Vyazmensky, A. (2008). *Numerical modelling of surface subsidence associated with block cave mining using a finite element/discrete element approach*. Ph.D. Thesis - Simon Fraser University.
- Vyazmensky, A., Elmo, D., & Stead, D. (2010). Role of rock mass fabric and faulting in the development of block caving induced surface subsidence. *Rock Mechanics and Rock Engineering*, 43(5), 533–556. <https://doi.org/10.1007/s00603-009-0069-6>
- Vyazmensky, A., Stead, D., Elmo, D., & Moss, A. (2010). Numerical analysis of block caving-induced instability in large open pit slopes: A finite element/discrete element approach. *Rock Mechanics and Rock Engineering*, 43(1), 21–39. <https://doi.org/10.1007/s00603-009-0035-3>
- Wang, X. (2005). Stereological interpretation of rock fracture traces on borehole walls and other cylindrical surfaces. *Faculty of the Virginia Polytechnic Institute and State University*, 113. <http://scholar.lib.vt.edu/theses/available/etd-09262005-164731/>
- Wellman, E. C., Annavarapu, S., Pratt, R. W., & Nicholas, D. E. (2012). Prediction of Fragmentation in Block Cave Mine Design – an update of the Core2Frag Program. *Massmin*.
- Yan, M. (2008). *Numerical Modelling of Brittle Fracture and Step-Path Failure : From Laboratory to Rock Slope Scale*. Ph.D Thesis - Simon Fraser University.
- Zhang, Z. X. (2002). An empirical relation between mode I fracture toughness and the tensile strength of rock. *International Journal of Rock Mechanics and Mining Sciences*, 39(3), 401–406. [https://doi.org/10.1016/S1365-1609\(02\)00032-1](https://doi.org/10.1016/S1365-1609(02)00032-1)